UCLA
UCLA Previously Published Works

Title

A three-dimensional misorientation axis- and inclination-dependent Kobayashi–Warren–Carter grain boundary model

Permalink

https://escholarship.org/uc/item/1zc8h5st

Authors

Admal, Nikhil Chandra
Segurado, Javier
Marian, Jaime

Publication Date

2019-07-01

DOI

10.1016/j.jmps.2019.03.020

Peer reviewed

A three-dimensional misorientation axis- and inclination-dependent Kobayashi–Warren–Carter grain boundary model

Nikhil Chandra Admal [a,b,*], Javier Segurado [c,d,a], Jaime Marian [a]

[a] *Materials Science and Engineering, University of California Los Angeles, United States*
[b] *Mechanical Science and Engineering, University of Illinois at Urbana-Champaign, United States*
[c] *IMDEA Materials Institute, Spain*
[d] *Department of Materials Science, Technical University of Madrid/Universidad Politécnica de Madrid, Spain*

ABSTRACT

The Kobayashi–Warren–Carter (KWC) phase-field model was originally conceived for two-dimensional systems to model grain boundary migration and grain rotation, which play a crucial role in nanocrystalline materials, and in phenomena such as superplasticity and recrystallization. Existing generalizations of the KWC model to three-dimensions construct the grain boundary energy as a function of misorientation angle between the grains, described as a scalar, and the inclination of the grain boundary. It is well-known that grain boundary energy is described on a five-dimensional space, where three dimensions describe misorientations and two describe inclinations. In this work, we generalize the KWC model by constructing a frame-invariant energy density that is sensitive to all the five-dimensions of misorientations and inclinations. In addition, we derive representations for energy density that result in different forms of anisotropies in inclination and misorientation. The developed framework enables us to introduce the effect of material symmetry on the inclination-dependence. We demonstrate the richness of the model using various three-dimensional numerical examples that simulate anisotropic grain coarsening and grain rotation.

Published by Elsevier Ltd.

1. Introduction

Interest in microstructure evolution models capable of capturing grain boundary kinetics has surged in recent times due to a renewed interest in dynamic phenomena in engineering materials mainly in the context of high-temperature applications. These developments have taken place at every scale, covering atomistic (Bulatov et al., 2013; Frolov et al., 2018a; 2018b; Janssens et al., 2006; Molodov et al., 2003; Molodov and Molodov, 2018; Olmsted et al., 2011; 2009; Wolf et al., 1992), mesoscopic (Anderson et al., 1984; Chen, 2002a; Han et al., 2018; Holm et al., 1991; Khater et al., 2012; Thomas et al., 2017; Upmanyu et al., 2006) and macroscopic continuum (Belytschko et al., 2009; Ma et al., 2006; Simone et al., 2006; Wei and Anand, 2004) scales, aided by critical advances in experimental characterization capabilities (e.g. Horita et al., 1998; Inkson et al., 2001; Kacher et al., 2011; Taheri et al., 2004; Taheri et al., 2010). While there are important aspects of the

---

* Corresponding author.
 E-mail address: admal@illinois.edu (N.C. Admal).

microstructure that require atomistic resolution to be studied properly, mesoscopic models are of particular interest because they operate on time and length scales that (i) are statistically significant to extract of *mean field* behavior, and (ii) facilitate direct comparison with experimental observations. These models typically subsume atomistic information into key parameters of the formulation that define the characteristic time and length constants, which can typically be orders of magnitude larger than those attainable directly by atomistic methods (ps and nm, respectively).

Among the most successful approaches belonging to this class of models is the *phase field* method, which tracks the evolution of different phases – each characterized by its own field variable – by following the principle of maximum dissipation of a free energy functional describing the state of the system (Chen, 2002a; Karma and Rappel, 1996; Steinbach et al., 1996). A system of coupled equations of motion – one for each field variable – discretized in space and time is then solved, leading to simulations of microstructural evolution. Within the phase field approach, otherwise sharp interfaces representing grain boundaries are spread over some arbitrarily small distance, effectively regularizing sharp discontinuities in the phase field and making the system amenable to numerical simulation (Chen, 2002a; Kobayashi et al., 1998; Krill Iii and Chen, 2002; Reina et al., 2014). For polycrystalline materials, the main two phase field approaches are the so-called *multiphase* field (MF) method (Chen and Yang, 1994; Garcke et al., 1999; Steinbach and Pezzolla, 1999; Steinbach et al., 1996) and the dual-phase method of Kobayashi et al. (1998, 2000) and Kobayashi and Giga (1999) (referred onwards as 'KWC'), and its variant developed by Henry et al. (2012). The MF method provides a robust platform for modeling grain evolution due to a number of advantageous features. For example, grain boundary energies and mobilities as functions of misorientation and inclination can be easily implemented (Kim et al., 2014; Mecozzi et al., 2016; Moelans et al., 2008a). As well, the method allows complete flexibility in terms of the number of orientation variables to capture arbitrary polycrystalline structures. Several of these capabilities have been recently adopted in a number of works, augmenting the applicability of the technique to a wide range of scenarios (e.g. see the review articles by Chen, 2002b; Hirouchi et al., 2012; Steinbach, 2009).

However, the MF method is limited by several shortcomings, chief among which are (i) the fact that the free energy of the system is not orientation invariant (which, for example, eliminates grain *rotation* as a feasible kinetic option) and (ii) the large potential computational cost associated with large numbers of evolving grains (Gránásy et al., 2004). These limitations are trivially solved by the KWC method, which allows for grain rotation and motion using a frame-independent free energy functional that depends only on two phase field variables, a structural one distinguishing between crystalline and disordered phases, and another that represents the crystal orientation field (Kobayashi et al., 1998; 2000). As well, we have recently showed that the KWC approach affords more flexibility for defining a unified variational framework within which to merge grain boundary kinetic processes with grain deformation (plastic) phenomena (Admal et al., 2018). A similar framework based on Cosserat crystal plasticity and the KWC constitutive model has been recently developed by Ask et al. (2018a,b). However, the KWC constitutive model is somewhat more rigid than MP methods when it comes to defining generalized free energies as a function of both grain misorientation and inclination, which limits its use to systems without anisotropic grain boundary energies. Indeed, to our knowledge, these extensions have thus far only been accomplished in the framework of the MP approach (Miyoshi and Takaki, 2016; Moelans et al., 2008b; Steinbach, 2009; Sursaeva and Straumal, 2005; Suwa and Saito, 2005), which prevents us from taking advantage of the beneficial aspects of the KWC model to simulate realistic microstructures.

Detailed constitutive information in the form of five-dimensional (5D) space of misorientation and inclination (i.e. alignment) dependent grain boundary energies has recently been produced by a number of computational studies (Bulatov et al., 2013; Kim et al., 2014; Olmsted et al., 2009; Runnels et al., 2016; Runnels, 2016). This points to the need to extend the KWC framework to account for this 5D space in a manner consistent with the key features of the model, i.e. maintaining frame indifference and restricting the number of phase field variables to the same two of the standard formulation. This is precisely the objective of this work.

Work augmenting KWC's capabilities to account for these extra complexities includes a three-dimensional generalization of the isotropic (i.e. the GB energy depending only on the misorientation angle) model using quaternions (Dorr et al., 2010; Kobayashi and Warren, 2005a; 2005b; Pusztai et al., 2005), and early consideration of the inclination dependence in the 2D model version (Kobayashi et al., 2000). However, to our knowledge, a full generalization in 3D of a model sensitive to the entire five-dimensional GB energy landscape has not been yet developed. In this paper, we provide such generalization by constructing a KWC functional where the expression for misorientation, described by the gradient of the scalar misorientation order parameter in the original model, is replaced by a frame-invariant tensorial quantity that encodes the misorientation axis, angle and the inclination of the grain boundary. Interestingly, from a crystal plasticity viewpoint, this tensor turns out to be the *geometrically necessary dislocation* (GND) tensor that results in a stress-free polycrystal. Therefore, our generalization preserves frame independence and introduces anisotropy in the misorientation axis between grains, effectively extending the free energy of the polycrystal to the combined 5D space of orientation/inclination.

The paper is organized as follows. First, we briefly review the KWC model and proceed to a three-dimensional generalization by expressing grain orientations using a rotation field. Beginning with a free energy density with an arbitrary dependence on the rotation field and it gradients, we arrive at constitutive restrictions on the functional form using the principle of material frame invariance. This result in the most general anisotropic KWC energy density that is sensitive to the five-dimensional space of misorientations and inclinations. In addition, we show further restrictions on the functional form of the generalized KWC energy density result in different flavors of anisotropy. We continue by demonstrating our approach in a few selected simulations of grain structure evolution, and finalize with a discussion and the conclusions.

N.C. Admal, J. Segurado and J. Marian / Journal of the Mechanics and Physics of Solids 128 (2019) 32–53

Notation: In this paper, we use direct and indicial notation whenever appropriate. In direct notation, we use uppercase and lowercase letters in bold to denote tensors and vectors respectively. $\mathbb{R}^n$ denotes the n-dimensional Euclidean space equipped with the standard inner product, and $\boldsymbol{e}^i (i = 1, \ldots, n)$ denote the standard basis vectors. The dot products are defined using the Einstein summation convention as $\boldsymbol{A} \cdot \boldsymbol{B} := A_{ij}B_{ij}$ and $\boldsymbol{u} \cdot \boldsymbol{v} = u_i v_i$, where $\boldsymbol{A}$ and $\boldsymbol{B}$ are tensors, while $\boldsymbol{u}$ and $\boldsymbol{v}$ are vectors. The transpose and determinant of a second-order tensor $\boldsymbol{A}$ are denoted by $\boldsymbol{A}^{\mathrm{T}}$ and $\det \boldsymbol{A}$ respectively. We use the notation $\alpha_{,i}$ and $\alpha_{,ij}$ to denote the partial derivatives $\partial \alpha / \partial X_i$ and $\partial \alpha / \partial X_i \partial X_j$ respectively. The gradient, divergence and Laplacian operators are denoted by ∇, Div and $\triangle$ respectively. Gradients of a scalar field α, a vector field $\boldsymbol{v}$, and tensor field $\boldsymbol{T}$ are first-, second- and third-order tensors defined as $[\nabla \alpha]_i := \alpha_{,i}$, $[\nabla \boldsymbol{v}]_{ij} := v_{i,j}$ and $[\nabla \boldsymbol{T}]_{ijm} := T_{ij,m}$ respectively. The tensor product of two vectors $\boldsymbol{a}$ and $\boldsymbol{b}$ is a second-order tensor $[(\boldsymbol{a} \otimes \boldsymbol{b})]_{ij} := a_i b_j$. The second-order antisymmetric tensor with axial vector $\boldsymbol{w}$, denoted by $[\boldsymbol{w} \times]$ is defined as $[\boldsymbol{w} \times]_{ij} := \epsilon_{ijm} w_m$. SO(3) denotes the set of all rotation tensors in three dimensions. The products $\boldsymbol{T}\mathcal{T}$ and $\mathcal{T}\boldsymbol{T}$ of a second-order tensor $\boldsymbol{T}$ and a third-order tensor $\mathcal{T}$ result in third-order tensors defined as $[\boldsymbol{T}\mathcal{T}]_{ijm} := T_{ip}\mathcal{T}_{pjm}$ and $[\mathcal{T}\boldsymbol{T}]_{ijm} := \mathcal{T}_{ijp}\boldsymbol{T}_{pm}$ respectively. The product of a fourth-order tensor $\mathbb{T}$ and a second-order tensor $\boldsymbol{T}$ is a second-order tensor given by $[\mathbb{T}\boldsymbol{T}]_{ij} = \mathbb{T}_{ijkl}T_{kl}$. ϵ_{ijk} denotes the three-dimensional Levi-Civita symbol.

2. The KWC model and the resulting grain boundary energy

The Kobayashi–Warren–Carter model proposed by Kobayashi et al. (1998, 2000) is a phase-field model to study grain evolution in polycrystalline materials. For two-dimensional polycrystals, the approach consists of two scalar order parameters ϕ and θ, representing, respectively, phase state and crystal orientation. ϕ ranges between 0 (disordered phase) and 1 (crystalline state), while θ represents the orientation of a crystal. The KWC free energy functional $\mathcal{W}^{\mathrm{KWC}}$ is given by

$$\mathcal{W}^{\mathrm{KWC}}[\phi, \theta] = \int_{\Omega} \psi^{\mathrm{KWC}}(\phi, \nabla\phi, \nabla\theta) \, d\boldsymbol{X}, \tag{1}$$

where $\Omega \subset \mathbb{R}^2$, and

$$\psi^{\mathrm{KWC}} = \frac{\alpha^2}{2} |\nabla\phi|^2 + f(\phi) + sg(\phi)|\nabla\theta| + \frac{\epsilon^2}{2} |\nabla\theta|^2, \tag{2}$$

with

$$f(\phi) = e(1-\phi)^2, \tag{3}$$

and $g(\phi)$ is an increasing function with $g(0) = 0$. Interestingly, a strikingly similar model was studied by Alicandro et al. (1999), albeit in a completely different context of fracture mechanics. In this paper, we choose

$$g(\phi) = -2(\ln(1-\phi) + \phi), \tag{4}$$

which was originally proposed by Kobayashi et al. (2000) in order to obtain a Read–Shockley type grain boundary energy dependence on the misorientation angle. In Appendix B, we demonstrate that $g(\phi) = \phi^2$, as chosen by Kobayashi et al. (1998, 2000), results in an incorrect evolution of grain boundaries, which may be reconciled using the results by Alicandro et al. (1999).

The resulting rate equations are given by

$$b^{\phi}\dot{\phi} = \alpha^2 \triangle \phi - sg'(\phi)|\nabla\theta| - f'(\phi), \tag{5a}$$

$$b^{\theta}\dot{\theta} = \mathrm{Div}\left[\epsilon^2 \nabla\theta + sg(\phi)\frac{\nabla\theta}{|\nabla\theta|}\right]. \tag{5b}$$

The steady state solution of Eq. (5) in 1D with Dirichlet boundary conditions on θ and ϕ describes a bicrystal with a flat grain boundary. As shown in Fig. 1, it is characterized by a constant θ in the bulk of the grains with a transition region at the grain boundary, and ϕ attains its minimum at the grain boundary signifying maximum disorder. Due to the presence of $|\nabla\theta|$ in the denominator, and $|\nabla\theta| = 0$ in the bulk of the grains, Eq. (5) is referred to as a *singular diffusive* equation. Therefore, solving Eq. (5) numerically requires that we approximate the total variation term $g(\phi)|\nabla\theta|$ in Eq. (2) to avoid the singularity mentioned above. In this paper, we use the approximation

$$g(\phi)|\nabla\theta| \approx g(\phi)\sqrt{|\nabla\theta|^2 + \rho^2}, \tag{6}$$

where ρ is a constant with units of inverse length, and numerically solve the resulting Euler–Lagrange equations. See ref. (Admal et al., 2018) for a physical interpretation of ρ.

Since the aim of this paper is to generalize the KWC model to describe a three-dimensional polycrystal with arbitrary grain orientations in SO(3), it is instructive to take a closer look at each term of the energy density given in Eq. (2). For simplicity assume $\epsilon = 0$. For a one-dimensional boundary-value problem in θ, a functional with integrand consisting of only the linear term $|\nabla\theta|$ (without $g(\phi)$) does not have a unique minimizer. On the other hand, for a given continuous function ϕ with a unique minimum in the interior of the domain, a functional constructed using $g(\phi)|\nabla\theta|$ has a unique minimizer
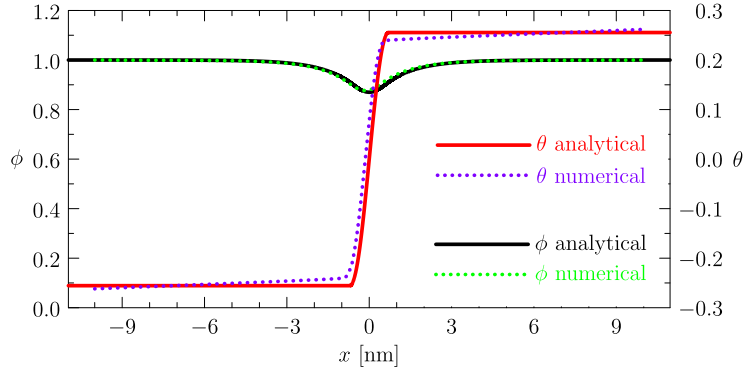
Fig. 1. Comparison of the steady state numerical solution to the steady state analytical solution given in Admal et al. (2018); Lobkovsky and Warren (2001) (adapted from Admal et al. (2018)). θ is expressed in units of radians.

in the set of all integrable functions on [0,1] with finite number of jumps.[1] This can be seen by noting that if $\phi(x_0)$ is the minimum of ϕ, then

$$
\int_0^1 g(\phi(x))|\nabla\theta|\,dx \geq g(\phi_0)\int_0^1 |\nabla\theta|\,dx
$$
$$
= g(\phi_0)|\theta(1) - \theta(0)|, \tag{7}
$$

with equality occurring only when θ is a step function with jump at x_0. In the presence of a non-zero ϵ, the steady state solution for θ is a smoothened step function, resulting in finite-sized grain boundary thickness. In addition to being a regularization parameter, Lobkovsky and Warren (2001) have shown that ϵ also plays an important role in furnishing a positive mobility to the grain boundary.

In what follows, we present a three-dimensional generalization of the KWC model with the orientation field θ of the 2D model replaced by a rotation field $R(X) \in SO(3)$. As mentioned in the introduction, existing works towards this goal are restricted to special cases, and to our knowledge, a generic model that is sensitive to the five-dimensional grain boundary space of misorientation and inclination has not yet been developed.

3. Generalization of the KWC functional to three-dimensional polycrystals

In this section, we generalize the KWC model to three dimensions. We begin by describing grain orientations using a smooth rotation field $R(X) \in SO(3)$, and constructing a frame-invariant free energy density density $\psi(\phi, \nabla\phi, R, \nabla R)$.

3.1. Material frame invariance

Let $\Omega \subset \mathbb{R}^3$ represent a polycrystal domain positioned in a Euclidean space $\mathbb{R}^3$, and X denotes an arbitrary point in Ω. In this section, we write the free energy density as $\psi(R, \nabla R)$, and suppress its dependence on ϕ and its gradients. Under a change of frame

$$
X^\star = QX, \quad Q \in SO(3), \tag{8}
$$

the rotation field transforms as

$$
R^\star(X) = QR(X). \tag{9}
$$

Therefore, frame-invariance of ψ implies

$$
\psi(R, \nabla R) = \psi(R^\star, \nabla^\star R^\star), \tag{10}
$$

where $\nabla^\star$ denotes the gradient operator with respect to $X^\star$. This implies

$$
\psi(R, \nabla R) = \psi(QR, Q(\nabla R)Q^{\mathrm{T}}) \quad \forall Q \in SO(3). \tag{11}
$$

For a fixed point $X \in \Omega$, choosing $Q = R^{\mathrm{T}}(X)$, we have

$$
\psi(R, \nabla R) = \psi(I, R^{\mathrm{T}}(\nabla R)R). \tag{12}
$$

Therefore, material frame invariance dictates that ψ is a function of the third-order tensor

$$
\mathcal{B}_{ijm} = [R^{\mathrm{T}}(\nabla R)R]_{ijm} = R_{ki}R_{kj,p}R_{pm}. \tag{13}
$$

---

[1] In higher dimensions, this set of functions is referred to as *special functions of bounded variation* originally proposed by De Giorgi and Ambrosio (1988).

Since $\boldsymbol{R} \in \mathrm{SO}(3)$, we have the identity $\boldsymbol{R}^{\mathrm{T}}\boldsymbol{R} \equiv \boldsymbol{I}$, which results in

$$R_{ki,p}R_{kj} + R_{ki}R_{kj,p} = 0. \tag{14}$$

Eq. (14) implies that $\mathcal{B}$ is antisymmetric in its first two indices, which enables us to contract $\mathcal{B}$ to a second-order tensor $\boldsymbol{B}$ as

$$B_{lm} = \epsilon_{lij}\mathcal{B}_{ijm}. \tag{15}$$

Alternately, let

$$\mathcal{G}_{ijm} := \frac{1}{2}\big[R_{ki}R_{km,p}R_{pj} - R_{ki}R_{kj,p}R_{pm}\big], \tag{16}$$

i.e. $\mathcal{G}$ is the anti-symmetric part of $\boldsymbol{R}^{\mathrm{T}}(\nabla\boldsymbol{R})\boldsymbol{R}$ in the last two indices. The following one-to-one relationships exist between $\mathcal{G}$ and $\mathcal{B}$:

$$\mathcal{B}_{ijm} = \mathcal{G}_{jim} - \mathcal{G}_{ijm} - \mathcal{G}_{mji}, \tag{17a}$$

$$\mathcal{G}_{ijm} = \frac{\mathcal{B}_{imj} - \mathcal{B}_{ijm}}{2}. \tag{17b}$$

Moreover, since $\mathcal{G}$ in anti-symmetric in two of its indices, it can be reduced to a second-order tensor $\boldsymbol{G}$ as

$$
\begin{aligned}
[\boldsymbol{G}]_{li} := \epsilon_{ljm}\mathcal{G}_{ijm} &= \frac{1}{2}\epsilon_{ljm}\big[R_{ki}R_{km,p}R_{pj} - R_{ki}R_{kj,p}R_{pm}\big] \\
&= -\frac{1}{2}\epsilon_{ljm}\big[R_{ki,p}R_{km}R_{pj} - R_{ki,p}R_{kj}R_{pm}\big] \\
&= -\frac{1}{2}R_{ki,p}\Big[\underbrace{\epsilon_{ljm}R_{km}R_{pj}}_{\epsilon_{qpk}R_{ql}(\det\boldsymbol{R})} - \underbrace{\epsilon_{ljm}R_{kj}R_{pm}}_{\epsilon_{qkp}R_{ql}(\det\boldsymbol{R})}\Big] \\
&= -R_{lq}^{\mathrm{T}}\epsilon_{qpk}R_{ik,p}^{\mathrm{T}} \\
&= -[\boldsymbol{R}^{\mathrm{T}}\mathrm{Curl}\,\boldsymbol{R}^{\mathrm{T}}]_{li}. \tag{18}
\end{aligned}
$$

From the above results, it follows that the third-order tensor $\boldsymbol{R}^{\mathrm{T}}(\nabla\boldsymbol{R})\boldsymbol{R}$ is completely described by the second-order tensor $\boldsymbol{R}^{\mathrm{T}}\mathrm{Curl}\,\boldsymbol{R}^{\mathrm{T}}$. Consequently, we have the following theorem

Theorem 1. *A function $\psi(\boldsymbol{R}, \nabla\boldsymbol{R})$ is frame-invariant if and only if it can be expressed as functions of any one of the second-order tensors $\boldsymbol{B}$ or $\boldsymbol{G}$, or the third-order tensors $\mathcal{B}$ or $\mathcal{G}$ defined in Eqs. (15), (18), (13) and (16) respectively.*

Interestingly, within the framework of crystal plasticity, $\boldsymbol{G}$ may be interpreted, as discussed in Appendix A, as the *geometrically necessary dislocation density* that results in a stress-free polycrystal. In the rest of the paper, a free energy density function is assumed to be frame-invariant.

3.2. Representation theorems for misorientation- and inclination-dependence

The results of the previous section describe an energy density that is material-frame indifferent. In this section, we explore different anisotropies of the grain boundary energy that result in different functional forms of $\boldsymbol{R}^{\mathrm{T}}\mathrm{Curl}\,\boldsymbol{R}^{\mathrm{T}}$.

A sharp-interface grain boundary between two grains is described by the orientations $\boldsymbol{R}^1$ and $\boldsymbol{R}^2 \in \mathrm{SO}(3)$ of two adjoining grains and the orientation of the grain boundary normal. Clearly, this representation is not unique as it is dependent on the choice of the observer. A grain boundary is uniquely described on a five-dimensional space characterized by the *misorientation* between the grains and the *inclination* of the grain boundary plane which we will now define such that they are frame-invariant. The misorientation between two adjoining grains with orientations $\boldsymbol{R}^1$ and $\boldsymbol{R}^2$ is given by $(\boldsymbol{R}^1)^{\mathrm{T}}\boldsymbol{R}^2$,[2] which is frame-invariant. On the other hand, inclination is described by the orientation of the grain boundary plane relative to the adjoining grains. Note the word *relative*, as it is incorrect to identify the grain boundary normal as a measure of inclination since it is not frame-invariant. Since misorientation is an arbitrary rotation, it accounts for three of the five dimensions of the GB space. On the other hand, since the orientation of the grain boundary plane can be described by a point on the unit sphere in $\mathbb{R}^3$, it accounts for the remaining two dimensions. In practice, the misorientation and inclination coordinates of the five-dimensional GB space are commonly used to describe grain boundary energies.

Mathematically, a flat grain boundary with a sharp-interface defined by a scalar misorientation angle θ_0, a misorientation axis represented as a unit vector $\bar{\boldsymbol{w}} \in \mathbb{R}^3$, and a grain boundary inclination $\bar{\boldsymbol{i}}$ can be described by a piecewise-constant rotation field given by

$$\boldsymbol{R}(\boldsymbol{X}; \theta_0, \bar{\boldsymbol{w}}, \bar{\boldsymbol{i}}) = \exp\{\theta(\boldsymbol{X}; \theta_0, \bar{\boldsymbol{i}})[\boldsymbol{w}\times]\}, \tag{19}$$

---

[2] The misorientation can equivalently be described by $(\boldsymbol{R}^2)^{\mathrm{T}}\boldsymbol{R}^1$.

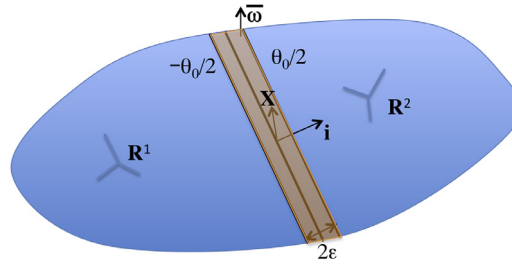**Fig. 2.** Diffuse-interface counterpart of a sharp-interface grain boundary, with a GB width of ε (see Eq. (23)).

where $\theta(\boldsymbol{X}; \theta_0, \bar{\boldsymbol{\imath}})$ is a piecewise-constant scalar-valued function

$$\theta(\boldsymbol{X}; \theta_0, \bar{\boldsymbol{\imath}}) = \begin{cases} -\theta_0/2 & \text{if } \boldsymbol{X} \cdot \bar{\boldsymbol{\imath}} < 0, \\ \theta_0/2 & \text{if } \boldsymbol{X} \cdot \bar{\boldsymbol{\imath}} \geq 0. \end{cases} \tag{20}$$

Eq. (19) describes a grain boundary located at the origin. Then, the grain boundary normal is given by the unit vector $\boldsymbol{n}$ that is parallel to $\nabla\theta$. The representation given in Eq. (19) results in $\boldsymbol{n} = \bar{\boldsymbol{\imath}}$, but this is certainly not true for a different frame.[3] Therefore, it is important to identify $\bar{\boldsymbol{\imath}}$ with inclination and not the grain boundary normal.

A diffuse-interface counterpart of the above-mentioned sharp-interface grain boundary, with a GB width of ε is represented in Fig. 2 and described by a smooth field $\boldsymbol{R}(\boldsymbol{X})$ given by

$$\boldsymbol{R}(\boldsymbol{X}; \epsilon, \theta_0, \bar{\boldsymbol{w}}, \bar{\boldsymbol{\imath}}) = \exp\{\theta(\boldsymbol{X}; \theta_0, \bar{\boldsymbol{\imath}})[\boldsymbol{w}(\boldsymbol{X}) \times]\}, \tag{22}$$

where $\theta(\boldsymbol{X}; \theta_0, \bar{\boldsymbol{\imath}})$ is a smoothened version of Eq. (20), given by

$$\theta(\boldsymbol{X}; \varepsilon, \theta_0, \bar{\boldsymbol{\imath}}) = \begin{cases} f\left(\frac{2\boldsymbol{X} \cdot \bar{\boldsymbol{\imath}}}{\varepsilon}\right)\frac{\theta_0}{2} & \text{if } 2\boldsymbol{X} \cdot \bar{\boldsymbol{\imath}} \in [-\varepsilon, \varepsilon], \\ -\theta_0/2 & \text{if } 2\boldsymbol{X} \cdot \bar{\boldsymbol{\imath}} < -\varepsilon, \\ \theta_0/2 & \text{if } 2\boldsymbol{X} \cdot \bar{\boldsymbol{\imath}} > \varepsilon, \end{cases} \tag{23}$$

constructed using a smooth continuous function $f : [-1, 1] \to [-1, 1]$ with $f(1) = -f(-1) = 1$, and $w : \mathbb{R}^3 \to S^2$ is a unit vector-valued function such that $\boldsymbol{w}(\boldsymbol{X}) = \bar{\boldsymbol{w}}$ if $2\boldsymbol{X} \cdot \bar{\boldsymbol{\imath}} \in \mathbb{R}\backslash(-\varepsilon, \varepsilon)$. By construction, the rotation field in Eq. (22) converges pointwise to Eq. (19) in the sharp-interface limit $\epsilon \to 0$. While the constant vectors $\bar{\boldsymbol{w}}$ and $\bar{\boldsymbol{\imath}}$ serve as non-local measures of misorientation and inclination, the fields $\boldsymbol{w}(\boldsymbol{X})$ and $\boldsymbol{R}^\mathrm{T}\nabla\theta/|\nabla\theta|$ qualify to be their respective local measures as they are frame-invariant.

From Section 3.1, we know that $\boldsymbol{G}$ serves as an invariant measure of grain boundary energy density. Therefore, we construct a grain boundary energy functional defined on the five-dimensional grain boundary space as

$$\mathcal{W}^\mathrm{KWC}[\boldsymbol{R}(\boldsymbol{X}; \epsilon, \theta_0, \bar{\boldsymbol{w}}, \bar{\boldsymbol{n}})] = \int \psi(\mathcal{B}) \, d\boldsymbol{X}, \tag{24}$$

where $\mathcal{B}$ is defined in Eq. (13). In order to construct a constitutive law from GB energy data obtained from an atomistic calculation, it is useful to identify the independent misorientation and inclination parts of $\mathcal{B}$, or equivalently $\boldsymbol{B}$ or $\boldsymbol{G}$, which enable us to explore anisotropic effects in misorientation and inclination independently. In other words, we are interested in exploring different invariance conditions, such as misorientation- or inclination-independence on $\mathcal{W}^\mathrm{KWC}$ that result in corresponding constitutive restrictions on ψ.

We begin with a transformation of the form

$$\boldsymbol{R} \to \boldsymbol{R}^\star := \boldsymbol{R}(\boldsymbol{X}; \theta_0, \bar{\boldsymbol{w}}, \boldsymbol{Q}\bar{\boldsymbol{\imath}}), \tag{25}$$

where $\boldsymbol{Q} \in \mathrm{SO}(3)$ is a constant rotation, which results in a rotation of the grain boundary plane while the misorientation remains fixed. The third-order tensor $\mathcal{B}$ transforms as

$$\mathcal{B}^\star = \mathcal{B}\boldsymbol{R}^\mathrm{T}\boldsymbol{Q}^\mathrm{T}\boldsymbol{R}, \tag{26}$$

and its second-order counterpart defined in Eq. (15) transforms as

$$\boldsymbol{B}^\star = \boldsymbol{B}\boldsymbol{R}^\mathrm{T}\boldsymbol{Q}^\mathrm{T}\boldsymbol{R}. \tag{27}$$

By construction, a free energy functional that satisfies

$$\mathcal{W}^\mathrm{KWC}[\boldsymbol{R}^\star] = \mathcal{W}^\mathrm{KWC}[\boldsymbol{R}]$$

---

[3] Note that under a change of frame $\boldsymbol{X}^\star = \boldsymbol{Q}\boldsymbol{X}$ for some $\boldsymbol{Q} \in \mathrm{SO}(3)$, and Eq. (19) transforms to

$$\boldsymbol{R}^\star(\boldsymbol{X}^\star) = \boldsymbol{Q}\boldsymbol{R}(\boldsymbol{Q}\boldsymbol{X}), \tag{21}$$

resulting in a grain boundary normal $\boldsymbol{Q}\boldsymbol{n}$.

is inclination-independent. Moreover since $\boldsymbol{Q}$ is arbitrary, $\boldsymbol{R}^T\boldsymbol{Q}^T\boldsymbol{R}$ in Eq. (27) is an arbitrary rotation. This motivates the following definition for the energy density.

Definition 1. A free energy density is said to be <u>inclination-independent</u> if it satisfies the condition

$$\psi(\boldsymbol{B}) = \psi(\boldsymbol{BQ}) \quad \forall \boldsymbol{Q} \in \text{SO}(3), \tag{28}$$

where $\boldsymbol{B}$ is defined in Eq. (15).

The following theorem characterizes the restrictions on the functional forms of an inclination-independent free energy density.

Theorem 2. *A free energy density ψ is inclination-independent if and only if it can be expressed as a function of $\boldsymbol{BB}^T$ or $\overline{\boldsymbol{G}}\,\overline{\boldsymbol{G}}^T$, where*

$$\overline{\boldsymbol{G}} := \boldsymbol{G} - \frac{1}{2}\text{Tr}(\boldsymbol{G})\boldsymbol{I}. \tag{29}$$

Proof. From Eq. (28), it is clear that any function of $\boldsymbol{BB}^T$ is inclination-independent. Conversely if a function $\psi(\boldsymbol{B})$ satisfies Eq. (28), then using the polar decomposition of $\boldsymbol{B} = \boldsymbol{V_B R_B}$, we have

$$\psi(\boldsymbol{B}) = \psi(\boldsymbol{V_B R_B Q}) \quad \forall \boldsymbol{Q} \in \text{SO}(3), \tag{30}$$

where $\boldsymbol{V_B} := \sqrt{\boldsymbol{BB}^T}$ and $\boldsymbol{R_B} \in \text{SO}(3)$. Note that if $\boldsymbol{B}$ is singular, then $\boldsymbol{R_B}$ is not unique. Nevertheless, a polar decomposition always exists. Choosing $\boldsymbol{Q} = \boldsymbol{R_B}^T$, we obtain

$$\psi(\boldsymbol{B}) = \psi(\boldsymbol{V_B}). \tag{31}$$

The rest of the proof is simple to complete if we show that $\boldsymbol{B} = -2\overline{\boldsymbol{G}}$. From the definition of $\boldsymbol{B}$, and the relationship between $\mathcal{B}$ and $\mathcal{G}$ given in Eq. (17a), we have

$$\begin{aligned} B_{lm} &= \epsilon_{lij}\mathcal{B}_{ijm} \\ &= \epsilon_{lij}(\mathcal{G}_{jim} - \mathcal{G}_{ijm} - \mathcal{S}_{mji}). \end{aligned} \tag{32}$$

Using the relation

$$\mathcal{G}_{ijm} = -\frac{1}{2}\epsilon_{jmn}G_{ni}, \quad \text{(from Eq. (18))} \tag{33}$$

Eq. (32) simplifies as

$$\begin{aligned} B_{lm} &= \frac{1}{2}\epsilon_{lij}(-\epsilon_{imn}G_{nj} + \epsilon_{jmn}G_{ni} + \epsilon_{jin}G_{nm}) \\ &= \frac{1}{2}[(\delta_{lm}G_{nn} - G_{lm}) + (\delta_{lm}G_{nn} - G_{lm}) + (G_{lm} - G_{lm}\delta_{ii})] \\ &= [-2\boldsymbol{G} + (\text{Tr}\boldsymbol{G})\boldsymbol{I}]_{lm} \\ &= -2\overline{\boldsymbol{G}}_{lm}. \end{aligned} \tag{34}$$

$\square$

We next proceed to explore misorientation axis-independent energy functionals using the transformation

$$\boldsymbol{R} \to \boldsymbol{R}^{\star\star}(\boldsymbol{X}) := \boldsymbol{R}(\boldsymbol{X}; \theta_0, \boldsymbol{Q}\bar{\boldsymbol{w}}, \bar{\boldsymbol{\imath}}), \tag{35}$$

which rotates the misorientation axis keeping the grain boundary inclination fixed. Under the transformation given in Eq. (35), $\boldsymbol{B}$ transforms as

$$\boldsymbol{B}^{\star\star} = \boldsymbol{Q}\boldsymbol{B}\boldsymbol{R}^T\boldsymbol{Q}\boldsymbol{R}\boldsymbol{Q}^T. \tag{36}$$

Analogous to Definition 1, we may now define a misorientation axis-independent free energy density with a function that satisfies the condition

$$\psi(\boldsymbol{B}) = \psi(\boldsymbol{Q}\boldsymbol{B}\boldsymbol{R}^T\boldsymbol{Q}\boldsymbol{R}\boldsymbol{Q}^T) \quad \forall \boldsymbol{Q} \in \text{SO}(3). \tag{37}$$

Unlike in Theorem 2, Eq. (37) *does not* result in an explicit restriction on ψ in terms of $\boldsymbol{B}$. Nevertheless, we propose an inclination-dependent functional form for ψ in Section 3.5 that 'weakly' depends on the misorientation axis. On the other hand, a grain boundary energy functional that is invariant with respect to transformations in Eqs. (25) and (35) is independent of the misorientation axis and inclination. The respective transformations of $\boldsymbol{B}$ given in Eqs. (28) and (37) motivate the following definition.

Definition 2. A grain boundary free energy density is said to be <u>isotropic</u> if it satisfies the condition

$$\psi(\boldsymbol{B}) = \psi(\boldsymbol{Q}\boldsymbol{B}) = \psi(\boldsymbol{B}\boldsymbol{Q}) \quad \forall \boldsymbol{Q} \in \text{SO}(3). \tag{38}$$

From Eq. (38), the following characterization of an isotropic grain boundary energy density follows.

Theorem 3. *A free energy density ψ is isotropic if and only if it can be expressed as a function of the invariants of $\boldsymbol{BB}^{\mathrm{T}}$, or equivalently $\boldsymbol{B}^{\mathrm{T}}\boldsymbol{B}$.*

Finally, we explore a mixed degree of freedom which we refer to as the *tilt angle*, defined as the angle between the misorientation axis and the grain boundary inclination. Interestingly, a result analogous to Theorem 2 exists for a KWC functional that only depends on the tilt and the misorientation angles. We see this by noting that such a KWC functional is invariant with respect to the transformation

$$\boldsymbol{R} \to \boldsymbol{R}(\boldsymbol{X}; \theta_0, \boldsymbol{Q}\bar{\boldsymbol{w}}, \boldsymbol{Q}\bar{\boldsymbol{\imath}}). \tag{39}$$

The transformation in Eq. (39) transforms $\boldsymbol{B}$ as

$$\boldsymbol{B} \to \boldsymbol{Q}\boldsymbol{B}\boldsymbol{Q}^{\mathrm{T}}, \tag{40}$$

which motivates the following definition.

Definition 3. A grain boundary free energy density is said to be <u>tilt-anisotropic</u> if it satisfies the condition

$$\psi(\boldsymbol{B}) = \psi(\boldsymbol{Q}\boldsymbol{B}\boldsymbol{Q}^{\mathrm{T}}) \quad \forall \boldsymbol{Q} \in \mathrm{SO}(3), \tag{41}$$

where $\boldsymbol{B}$ is defined in Eq. (15).

By definition, every isotropic grain boundary is trivially tilt-anisotropic. From Eq. (39), we have the following characterization of a tilt-anisotropic grain boundary energy density.

Theorem 4. *A free energy density ψ is tilt-anisotropic if and only if it can be expressed as a function of the invariants of $\boldsymbol{B}$ or $\overline{\boldsymbol{G}}$, where $\overline{\boldsymbol{G}}$ is defined in Eq. (29).*

3.3. A three-dimensional isotropic KWC energy functional

In this section, we construct an isotropic KWC energy functional. From Theorem 3, we know that an isotropic grain boundary energy density is a function of the invariants of $\overline{\boldsymbol{G}}\,\overline{\boldsymbol{G}}^{\mathrm{T}}$. Since the co-existence of a linear and a quadratic term in the gradient of rotation is the essential feature of the KWC energy density (see Eq. (2)) that results in grain boundaries, we begin by considering the following function for the energy density:

$$\psi^{\mathrm{KWC}} = \frac{\alpha^2}{2}|\nabla\phi|^2 + f(\phi) + sg(\phi)\sqrt{\overline{\boldsymbol{G}}\cdot\overline{\boldsymbol{G}}} + \frac{\epsilon^2}{2}\overline{\boldsymbol{G}}\cdot\overline{\boldsymbol{G}}, \tag{42}$$

where $\overline{\boldsymbol{G}}$ is defined in Eq. (29). In order to explicitly see the misorientation axis- and inclination-independence, we first note that

$$\begin{aligned}
\overline{\boldsymbol{G}}\cdot\overline{\boldsymbol{G}} &= \frac{1}{4}\boldsymbol{B}\cdot\boldsymbol{B} \\
&= \frac{1}{2}\mathcal{B}\cdot\mathcal{B} \\
&= \frac{1}{2}\nabla\boldsymbol{R}\cdot\nabla\boldsymbol{R}.
\end{aligned} \tag{43}$$

Using the rotation field given in Eq. (22), we have

$$\begin{aligned}
R_{ij,m}R_{ij,m} &= R_{ik}[\theta\boldsymbol{w}\times]_{kj,m}R_{il}[\theta\boldsymbol{w}\times]_{lj,m} \\
&= [\theta\boldsymbol{w}\times]_{kj,m}[\theta\boldsymbol{w}\times]_{kj,m} \\
&= \epsilon_{kjl}(\theta w_l)_{,m}\,\epsilon_{kjm}(\theta w_m)_{,m} \\
&= 2|\nabla(\theta\boldsymbol{w})|^2 \\
&= 2(|\nabla\theta|^2 + \theta^2|\nabla\boldsymbol{w}|^2),
\end{aligned} \tag{44}$$

where in the last equality we used the condition $\nabla\boldsymbol{w}^{\mathrm{T}}\boldsymbol{w}\equiv 0$ since $|\boldsymbol{w}| = 1$. Substituting Eq. (44) into Eq. (43), we have

$$\overline{\boldsymbol{G}}\cdot\overline{\boldsymbol{G}} = |\nabla\theta|^2 + \theta^2|\nabla w|^2. \tag{45}$$

The energy density simplifies to a function of ϕ, θ, $\nabla\theta$ and $\nabla\boldsymbol{w}$ as follows

$$\begin{aligned}
\widetilde{\psi}^{\mathrm{KWC}}(\phi, \theta, \nabla\theta, \nabla\boldsymbol{w}) = \\
\frac{\alpha^2}{2}|\nabla\phi|^2 + f(\phi) + sg(\phi)\sqrt{|\nabla\theta|^2 + \theta^2|\nabla w|^2} + \frac{\epsilon^2}{2}(|\nabla\theta|^2 + \theta^2|\nabla w|^2).
\end{aligned} \tag{46}$$

It is straightforward to see that a solution of the resulting Euler–Lagrange equation with boundary conditions[4] $\theta(0) = 0$, $\theta(L) = \overline{\theta}$ and $\boldsymbol{w}(0) = \boldsymbol{w}(L) = \overline{\boldsymbol{w}}$ is in fact given by $\phi(\boldsymbol{X})$ and $\theta(\boldsymbol{X})$ (see equations A.10 and A.11 in Admal et al., 2018) that solve the Euler–Lagrange equations of the 1D KWC problem given in Eq. (5), with

$$\boldsymbol{w}(X) \equiv \overline{\boldsymbol{w}}. \tag{47}$$

The energy functional given in Eq. (46) was first constructed by Kobayashi and Warren (2005a,b) and Pusztai et al. (2005), and implemented using Rodrigues vectors and quaternion representations of orthogonal tensors respectively. We now make the following interesting observations:

- The steady-state 1D solution given in Eq. (47) is a geodesic in SO(3) connecting $\boldsymbol{R}^1$ and $\boldsymbol{R}^2$. It is well-known that the linear term $|\nabla w|$ (without the coefficient $sg(\phi)$) in Eq. (46) determines the geodesic uniquely up to parametrization, while the remaining terms in Eq. (46) determine the parametrization uniquely.
- A geodesic on a Riemannian manifold is determined by its metric. The metric on the tangent space of SO(3) in the above one-dimensional example is given by Eq. (45). This metric is commonly referred to as a bi-invariant metric due to its invariance with respect to the transformations in Eq. (25) (left-invariance) and a transformation (right-invariance) of the form $\boldsymbol{R} \rightarrow \boldsymbol{RQ}$.
- Using Eq. (47), we have the following expression for $\boldsymbol{G}$

$$\begin{aligned} \boldsymbol{G} &= \boldsymbol{R}^{\mathrm{T}} \mathrm{Curl} \boldsymbol{R}^{\mathrm{T}} \\ &= \boldsymbol{R}^{\mathrm{T}} (\nabla \theta \times) \boldsymbol{RW} \\ &= \left[\left(\boldsymbol{R}^{\mathrm{T}} \nabla \theta \right) \times \right] \boldsymbol{W} \\ &= \boldsymbol{w} \otimes \boldsymbol{R}^{\mathrm{T}} \nabla \theta - \left(\boldsymbol{w} \cdot \boldsymbol{R}^{\mathrm{T}} \nabla \theta \right) \boldsymbol{I}, \end{aligned} \tag{48}$$

which implies

$$\overline{\boldsymbol{G}} = \boldsymbol{w} \otimes \boldsymbol{R}^{\mathrm{T}} \nabla \theta. \tag{49}$$

Note that the above expression is valid only for a uniform $\boldsymbol{w}$.

3.4. A misorientation-anisotropic and inclination-isotropic KWC functional

In this section, we generalize the constitutive law given in Eq. (42) to include anisotropy in misorientation-axis while being isotropic in inclination. From Section 3.2, we know that such a free energy density should be a function of $\overline{\boldsymbol{G}}\boldsymbol{G}^{\mathrm{T}}$. Therefore, we consider the following KWC free energy density:

$$\psi^{\mathrm{KWC}} = \frac{\alpha^2}{2} |\nabla \phi|^2 + f(\phi) + sg(\phi) \sqrt{\mathbb{T} \overline{\boldsymbol{G}} \cdot \overline{\boldsymbol{G}}} + \frac{\epsilon^2}{2} \mathbb{T} \overline{\boldsymbol{G}} \cdot \overline{\boldsymbol{G}}, \tag{50}$$

where $\mathbb{T}$ is a fourth-order positive-definite symmetric tensor. $\mathbb{T}$ characterizes the anisotropy in the choice of misorientation axis. If $\mathbb{T}$ is an identity tensor, then Eq. (50) reduces to the isotropic case given in Eq. (42).

In 1D, the term $\sqrt{\mathbb{T} \overline{\boldsymbol{G}} \cdot \overline{\boldsymbol{G}}}$ reduces to a metric on SO(3). Due to its invariance with respect to the transformation $\boldsymbol{R} \rightarrow \boldsymbol{QR}$ ($\boldsymbol{Q} \in$ SO(3)), it is commonly referred to as a left-invariant metric on the Lie group SO(3).[5] It is well known, and succinctly shown by Zefran et al. (1996), that geodesics in SO(3) are of the form $\exp(\theta(\boldsymbol{X})[\boldsymbol{w} \times])$, where $\boldsymbol{w}$ is a constant unit vector, if and only if the metric is a biinvariant metric of the form $\overline{\boldsymbol{G}}\boldsymbol{G}^{\mathrm{T}}$. Therefore, we do not expect the minimizer of Eq. (50) for a given boundary value problem to have a constant $\boldsymbol{w}$ unlike in Eq. (47). This observation also highlights the generality of the approach used to obtain the characterization given in Theorem 2, as one may conclude the same for a special case of constant $\boldsymbol{w}$ by noting from Eq. (49) that $\overline{\boldsymbol{G}}\boldsymbol{G}^{\mathrm{T}} = |\nabla \theta|^2 \boldsymbol{w} \otimes \boldsymbol{w}$ is independent of $\boldsymbol{n}$. In this paper, we do not pursue any analytical solutions. Instead, we will demonstrate certain features of the solutions of boundary value problems using numerics in Section 4.

3.5. A KWC energy functional with anisotropy in inclination

In this section, we explore the possibility of constructing a misorientation-axis independent free energy density. From Section 3.2, recall that our framework does not give rise to a restriction on ψ as a function of $\boldsymbol{B}$ or $\overline{\boldsymbol{G}}$. Nevertheless, for a constant misorientation axis, Eq. (49) implies

$$\overline{\boldsymbol{G}}^{\mathrm{T}} \overline{\boldsymbol{G}} / \overline{\boldsymbol{G}} \cdot \overline{\boldsymbol{G}} = \boldsymbol{R}^{\mathrm{T}} \boldsymbol{n} \otimes \boldsymbol{R}^{\mathrm{T}} \boldsymbol{n}, \tag{51}$$

---

[4] These boundary condition are equivalent to the boundary conditions $\boldsymbol{R}(0) = \boldsymbol{I}$, and $\boldsymbol{R}(L) = \exp([\overline{\theta}\overline{\boldsymbol{w}} \times])$, where $\overline{\theta} \in \mathbb{R}$ and $\overline{\boldsymbol{w}}$ are constant scalar and unit vector respectively.

[5] Geodesics of left-invariant metrics were first studied by Vladimir Arnold in a famous article (Arnold, 1966) which demonstrates similarities between the motion of a rigid body and the motion of an incompressible inviscid fluid.

which describes inclination-dependence with a weak dependence on the misorientation axis. By weak, we mean that in the sharp interface limit, $\theta(\boldsymbol{X})$ converges to a step function which results in $\boldsymbol{R}^{\mathrm{T}}\nabla\boldsymbol{n} \to \delta_{\boldsymbol{X}=\boldsymbol{0}}\boldsymbol{n}$, which is independent of the choice of $\boldsymbol{w}$. Therefore, although $\boldsymbol{R}^{\mathrm{T}}\boldsymbol{n}$ depends on $\boldsymbol{w}$ through $\boldsymbol{R}$, its dependence vanishes in the sharp-interface limit. Assuming constant $\boldsymbol{w}$, Eq. (51) results in

$$\boldsymbol{R}^{\mathrm{T}}\boldsymbol{n} = \sqrt{\mathrm{diag}(\overline{\boldsymbol{G}}^{\mathrm{T}}\overline{\boldsymbol{G}})/\overline{\boldsymbol{G}} \cdot \overline{\boldsymbol{G}}}, \tag{52}$$

which implies $\boldsymbol{R}^{\mathrm{T}}\boldsymbol{n}$ is frame-invariant as it can be expressed as a function of $\overline{\boldsymbol{G}}$. Note that we arrived at Eq. (52) assuming a constant $\boldsymbol{w}$. For a non-constant $\boldsymbol{w}$, we view Eq. (52) as a definition.

Therefore, we propose the following KWC energy density that depends weakly on the misorientation-axis:

$$\psi^{\mathrm{KWC}}(\phi, \nabla\phi, \overline{\boldsymbol{G}}) = \frac{\alpha^2}{2}|\nabla\phi|^2 + f(\phi) + sg(\phi)h(\boldsymbol{R}^{\mathrm{T}}\boldsymbol{n})|\overline{\boldsymbol{G}}| + \frac{\epsilon^2}{2}|\overline{\boldsymbol{G}}|^2, \tag{53}$$

where $\boldsymbol{R}^{\mathrm{T}}\boldsymbol{n}$ is given by Eq. (52). The function $h : S^2 \to \mathbb{R}$ describes the anisotropy in inclination with $\boldsymbol{R}^{\mathrm{T}}\boldsymbol{n}$ being the measure of inclination. To better understand the inclination measure $\boldsymbol{R}^{\mathrm{T}}\boldsymbol{n}$, consider a tilt boundary with misorientation axis along the $\boldsymbol{e}^3$ direction constructed using a smooth rotation field $\boldsymbol{R}(\boldsymbol{X}_1) = \exp(\theta(X_1)\boldsymbol{e}^3)$, where $\theta(X_1)$ transitions from $-\theta_0/2$ to $\theta_0/2$ across the grain boundary. Although the grain boundary normal $\nabla\theta/|\nabla\theta| = (1, 0, 0)$ is constant, the inclination measure $\boldsymbol{R}^{\mathrm{T}}\nabla\theta/|\nabla\theta|$ indicates the inclination is diffused in a neighborhood of $(1,0,0)$ in S^2. On the other hand, in the case of a pure twist boundary, since $\boldsymbol{R}^{\mathrm{T}}\boldsymbol{n} = \boldsymbol{n}$, the inclination does not get diffused. We will revisit this observation in Section 4.2.

3.6. A tilt-anisotropic KWC energy functional

In this section, we construct a tilt-anisotropic KWC energy density. From Section 3.2, recall that a tilt-anisotropic grain boundary energy depends on the misorientation axis and the grain boundary inclination only through the angle between them, and it is characterized by an energy density that is a function of the invariants of $\boldsymbol{B}$ or $\overline{\boldsymbol{G}}$. Therefore, we consider the following energy density with anisotropy described by the trace of $\overline{\boldsymbol{G}}$:

$$\psi^{\mathrm{KWC}} = \frac{\alpha^2}{2}|\nabla\phi|^2 + f(\phi) + sg(\phi)\bar{h}(\Theta)\sqrt{\overline{\boldsymbol{G}} \cdot \overline{\boldsymbol{G}}} + \frac{\epsilon^2}{2}\overline{\boldsymbol{G}} \cdot \overline{\boldsymbol{G}}. \tag{54}$$

where the Θ represents the tilt angle. From Eq. (49), we know that $\overline{\boldsymbol{G}} \cdot \boldsymbol{I} = \boldsymbol{w} \cdot \boldsymbol{n}$ whenever $\boldsymbol{w}(\boldsymbol{X})$ is uniform. Therefore, we define the tilt angle in the non-uniform setting as

$$\Theta := \begin{cases} \arccos\left(\frac{\overline{\boldsymbol{G}} \cdot \boldsymbol{I}}{|\overline{\boldsymbol{G}}|}\right) & \text{if } |\overline{\boldsymbol{G}}| \neq 0, \\ 0 & \text{otherwise.} \end{cases} \tag{55}$$

Note that although Θ in Eq. (55) is defined by identifying the tilt angle for a specialized case of uniform $\boldsymbol{w}$, the energy density given in Eq. (54) is applicable for the general case where $\boldsymbol{w}$ may be varying across the grain boundary. This is because, we know from Theorem 4 that the energy density in Eq. (54) is tilt-anisotropic as it depends on the two invariants, $\overline{\boldsymbol{G}} \cdot \boldsymbol{I}$ and $|\overline{\boldsymbol{G}}|$, of $\overline{\boldsymbol{G}}$. We refer to the function $\bar{h}$ as a tilt-anisotropy function.

We end Section 3 by noting the following striking differences between the current model and those developed by Kobayashi et al. (2000) and Pusztai et al. (2005). In our model the anisotropy is completely described by the rotation field through the functions $\sqrt{\mathbb{T}\overline{\boldsymbol{G}} \cdot \boldsymbol{G}}$ or $h(\boldsymbol{G})$, whereas the inclination anisotropy in Kobayashi et al. (2000) was constructed using the gradients of ϕ. In addition, we *do not* take into account crystal symmetries.[6] For their part, Pusztai et al. (2005) incorporate crystal symmetries into their 3D isotropic model that simulates solid crystals nucleating and growing in a liquid melt by having $\epsilon = 0$ and using the finite difference method. Since taking $\epsilon = 0$ results in discontinuities in the orientation of the order parameter, it was possible for Pusztai et al. (2005) to incorporate crystal symmetries into the model by accounting for the jump in orientation. However, it is well known that $\epsilon = 0$ results in zero mobility for grain boundaries in the absence of liquid melt. Since the current paper is focused on grain boundary motion in solids, such an approach cannot be adopted into our framework.

4. Numerical examples

In this section, we numerically study the isotropic and the various anisotropic models developed in Section 3. We use the angle-axis representation to express an arbitrary rotation $\widehat{\boldsymbol{R}}$ as a three dimensional vector $\boldsymbol{q}$, where

$$\widehat{\boldsymbol{R}}(\boldsymbol{q}) = \boldsymbol{I} + \frac{\sin|\boldsymbol{q}|}{|\boldsymbol{q}|}\boldsymbol{W} + \frac{1}{2}\left[\frac{\sin(|\boldsymbol{q}|/2)}{(|\boldsymbol{q}|/2)}\right]^2\boldsymbol{W}^2, \tag{56}$$

---

[6] For example, a misorientation of 90° in a cubic crystal does not result in a grain boundary.

Table 1

KWC parameters used in the implementation of various models used in the paper.

	$g(\phi) = -2(\log(1 - \phi) + \phi)$
ϵ^2/χ	3.1999×10^{-10} Jm^{-1}
α^2/χ	7.95×10^{-9} Jm^{-1}
s	0.85Jm^{-1}
$e\chi$	3.5×10^{8} Jm^{-3}
b^ϕ	1×10^{12} Js/m^3
$m^{\boldsymbol{q}}_{\max}$	1×10^{-15} m^3/(Js)
$m^{\boldsymbol{q}}_{\min}$	1×10^{-21} m^3/(Js)
ρ^2	1×10^{13} m^{-2}

and $\boldsymbol{W}$ is the skew-symmetric tensor associated with $\boldsymbol{q}$, i.e. $\boldsymbol{W} = [\boldsymbol{q}\times]/|\boldsymbol{q}|$. In this representation, the magnitude and direction of $\boldsymbol{q}$ represent the misorientation angle and axis respectively. The representation in Eq. (56) allows us to express the rotation field in terms of the field $\boldsymbol{q}(\boldsymbol{X})$ as

$$\boldsymbol{R}(\boldsymbol{X}) = \widehat{\boldsymbol{R}}(\boldsymbol{q}(\boldsymbol{X})). \tag{57}$$

Substituting Eq. (57) into the functionals developed in Section 3 recasts them into functionals of $\boldsymbol{q}(\boldsymbol{X})$ and $\phi(\boldsymbol{X})$. Subsequently, taking variations with respect to $\boldsymbol{q}$ and ϕ, results in the following Euler–Lagrange equations:

$$b^{\boldsymbol{q}}\dot{\boldsymbol{q}} = \delta_{\boldsymbol{q}}\mathcal{W}^{\text{KWC}},$$
$$b^\phi\dot{\phi} = \delta_\phi\mathcal{W}^{\text{KWC}}, \tag{58}$$

where b^ϕ and $b^{\boldsymbol{q}}$ are scalar inverse mobilities for the order parameters ϕ and $\boldsymbol{q}$ respectively, and $\delta_\square$ denotes variation with respect to $\square$. Recall that the weighted total residual term that appears in the two-dimensional KWC model, discussed in Section 2, results in a singular diffusive equation. Analogously, the weighted linear term $\sqrt{\boldsymbol{G}\cdot\boldsymbol{G}}$ appearing in Eqs. (42) and (54), or $\sqrt{\mathbb{T}\boldsymbol{G}\cdot\boldsymbol{G}}$ appearing in Eq. (50) also result in singular-diffusive equations. Therefore, we use Eq. (6) to approximate the square root function as discussed in Section 2. The material parameters common to all the models are listed in Table 1. These material parameters are chosen and scaled[7] to result in a GB thickness that can be supported by a finite element mesh.

The Euler–Lagrange equations resulting from Eq. (58) along with appropriate boundary conditions are numerically solved for using the finite element method. The initial condition on ϕ in all simulations that follow is chosen as

$$\phi(\boldsymbol{X}, 0) \equiv 1, \tag{59}$$

while the function

$$\theta(\boldsymbol{X}; \theta_0) = -\theta_0\left(\frac{1}{2} + \frac{1}{1 + \exp(-2.5X_1)}\right), \tag{60}$$

where θ_0 denotes the misorientation angle, is used to construct an appropriate initial condition on $\boldsymbol{q}$ in simulations involving bicrystals. Boundary conditions on ϕ and $\boldsymbol{q}$, whenever applicable, are chosen as

$$\phi(\partial\Omega, t) = 1, \quad \boldsymbol{q}(\partial\Omega, t) = \boldsymbol{q}(\partial\Omega, 0), \tag{61}$$

unless otherwise noted. The unknown fields ϕ and $\boldsymbol{q} = (q_1, q_2, q_3)$ are interpolated using triangular (in 2D) or tetrahedral (in 3D) Lagrange quadratic finite elements. Eq. (58) are solved using the MUMPS direct solver with Anderson acceleration, and BDF (Backward Differential Formula) time stepping algorithm implemented in COMSOL5.2.

4.1. A parametric study of an inclination-independent energy functional

In order to demonstrate the anisotropy in misorientation-axis resulting due to Eq. (50), we perform a parametric study of the steady-state grain boundary energy resulting in a one-dimensional bicrystal with a fixed misorientation angle $\theta_0 = 60°$, and misorientation axis parametrized by angles $\gamma_a \in [0, \pi/2]$ and $\gamma_p \in [0, 2\pi]$ representing the azimuth (with z-axis describing the zenith) and polar angles respectively. The 1D bicrystal is represented by the segment $[-10\,\text{nm}, 10\,\text{nm}]$, with a diffused grain boundary of misorientation angle $40°$ positioned at the origin. The initial conditions for $\boldsymbol{q}$ are expressed in terms of the parameters γ_a and γ_p as

$$q_1(X_1, 0) = \theta(X_1; \theta_0)\cos(\gamma_p)\sin(\gamma_a),$$
$$q_2(X_1, 0) = \theta(X_1; \theta_0)\sin(\gamma_p)\sin(\gamma_a),$$
$$q_3(X_1, 0) = \theta(X_1; \theta_0)\cos(\gamma_a),$$

---

[7] See Lobkovsky and Warren (2001) for scaling of the KWC material parameters that preserves GB energy but changes the GB thickness.
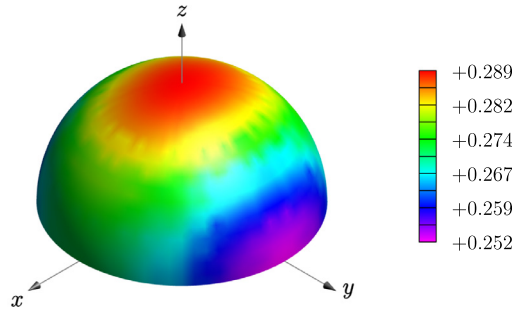
Fig. 3. A spherical polar plot of the steady-state grain boundary energy in Jm^{-2} of a 1D bicrystal computed using the energy density, given in Eq. (50), with **T** shown in Eq. (63). (For interpretation of the references to color in the text, the reader is referred to the web version of this article.)

which essentially imply that the misorientation axis is parametrized by the angles γ_a and γ_p while the inclination of the grain boundary at the origin is fixed. The anisotropy in misorientation is fixed using the form

$$\mathbb{T}_{ijkl} = T_{ik} \boldsymbol{I}_{jl}, \tag{62}$$

where **T** is a second-order positive-definite symmetric tensor,

$$\boldsymbol{T} = \begin{bmatrix} 1.0 & 0 & 0 \\ 0 & 0.8 & 0 \\ 0 & 0 & 1.2 \end{bmatrix}, \tag{63}$$

and **I** is the second-order identity tensor, resulting in $\mathbb{T}\bar{\boldsymbol{G}} = \boldsymbol{T}\bar{\boldsymbol{G}}$. The degree of anisotropy depends on the condition number of **T** which ultimately decides the stability of the descretized problem. In this paper, we choose a mild anisotropy as our focus is not on addressing the stability of the numerical method.[8] The domain is discretized using a uniform mesh of 50 elements, and the system is evolved for 1s.

A polar plot of the resulting grain boundary energy is shown in Fig. 3, where a vector joining the origin to a point in the hemisphere describes the misorientation axis, and the color scale describes the GB energy. In this paper, we do not pursue the precise relationship between the anisotropies in **T** and the grain boundary energy, but it is clear from Eq. (63) and Fig. 3 that the eigenvectors and the anisotropy of the eigenvalues of **T** correspond to the misorientation axis and grain boundary energy anisotropy respectively. We did not explore inclination isotropy in this section since the free energy density in Eq. (50) results in inclination isotropy by construction.

4.2. Simulations demonstrating inclination anisotropy

In this section, we present a numerical study of the KWC energy given in Eq. (53) which describes inclination anisotropy with a weak-dependence on misorientation-axis. Recall from Section 3.5, by weak-dependence, we mean that in the absence of variations in the misorientation axis across the grain boundary, the sharp-interface limit of the model is independent of the choice of the misorientation axis.

We begin with two parametric studies, one exploring inclination anisotropy, and the other the extent of misorientation axis-anisotropy since the model, as noted in Section 3.5, is not strictly isotropic with respect to the misorientation axis. We consider a 1D bicrystal which is represented by the segment [10 nm, 10 nm], with a diffused grain boundary of misorientation angle $\theta_0 = 40°$ positioned at the origin. The inclination anisotropy function h chosen for this study is

$$h(\boldsymbol{n}) = 1.2 - 0.2 \sin^2(2\phi) \sin^2(2\theta), \tag{64}$$

where θ and ϕ are the azimuth and polar angles (with z-axis describing the zenith) given by $\cos\theta = n_1/\sqrt{n_1^2 + n_2^2}$ and $\cos\phi = n_3$ respectively. See Fig. 4 for a polar plot of h.

In order to explore inclination anisotropy, we compute the grain boundary energies of bicrystals with varying inclinations, and a fixed misorientation axis. A bicrystal with a flat grain boundary is constructed with grain boundary normal described by a unit vector on S^2, and parametrized using an azimuth angle γ_a (with z-direction chosen as the zenith), and a polar angle γ_p. The above-mentioned construction can be equivalently conceived in 1D by changing the reference frame to fix the grain boundary normal parallel to the x-axis, and expressing the rotation field (instead of Eq. (57)) as

$$\boldsymbol{R}(\boldsymbol{X}, t) = \boldsymbol{Q}(\gamma_a, \gamma_p)\widehat{\boldsymbol{R}}(\boldsymbol{q}(\boldsymbol{X}, t)), \tag{65}$$

where **Q** is a rotation that maps the unit vector described by the angles γ_a and γ_p to $\boldsymbol{e}_1$. Initial conditions on $\boldsymbol{q}$ are chosen as

$$q_3(X_1) = \theta(X_1; \theta_0); q_1 \equiv q_2 \equiv 0, \tag{66}$$

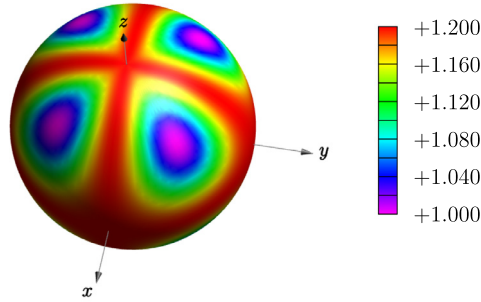[8] We would like to thank one of the Reviewer for identifying this challenge.

Fig. 4. A polar plot of the anisotropic function h given in Eq. (64). It is symmetric about the *xy, yz* and the *xz* planes. (For interpretation of the references to color in the text, the reader is referred to the web version of this article.)
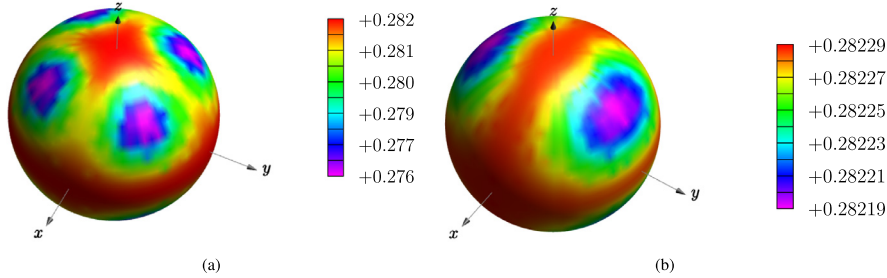

(a)   (b)

Fig. 5. Polar plots of grain boundary energies in Jm^{-2} computed using the inclination-dependent grain boundary model given in Eq. (53). In (a), the misorientation axis is fixed along the *z*-direction while the varying GB inclination is described as a unit vector on the sphere. (b) corresponds to a grain boundary with fixed inclination $\boldsymbol{R}^{\mathrm{T}}(0, t)\boldsymbol{n}$, with varying misorientation axis described as a unit vector on the sphere.

which ensure the misorientation axis is along the *z*-axis. For example, $(\gamma_a, \gamma_p) = (\pi/2, 0)$ results in $\boldsymbol{Q} = \boldsymbol{I}$, and corresponds to a tilt grain boundary, while $(\gamma_a, \gamma_p) = (0, 0)$[9] results in a twist boundary. Also note the distinction between inclination, described by a unit vector in terms of the azimuth and polar angles, and the grain boundary normal.

Substituting Eq. (65) into the energy density given in Eq. (53) results in an inclination-dependent energy functional in 1D that is parametrized by $\gamma_a \in [0, \pi/2]$ and $\gamma_p = [0, 2\pi]$. The domain in discretized using a uniform mesh of 50 elements, and the parametric space is discretized uniformly with a grid size of 5°. For each pair of parametric angles discretized in steps of 5°, we evolve the resulting Euler–Lagrange equations subject to the initial conditions given in Eqs. (66) and (59), and boundary conditions given in Eq. (61) for 1s in order to reach the corresponding steady states. Fig. 5a shows a polar plot of the grain boundary energy with the unit vector on the sphere describing the grain boundary inclination. The plot clearly shows that the patterns of maxima and minima in the polar plot match that of the polar plot of the anisotropic function. We also note that the anisotropy in the grain boundary energy is not as pronounced as in the anisotropic function which may be reasoned by an analytical study of the grain boundary energy.[10] We do not pursue this further in this paper.

We next perform a parametric study of the 1D bicrystal described above by fixing the inclination at the origin to be along the *x*-axis and misorientation angle at 40° while varying the misorientation-axis. The aim here is to explore the extent of anisotropy in misorientation. The misorientation axis is parametrized using the azimuth and polar angles γ_a and γ_p. Using the representation given in Eq. (57), we solve the Euler–Lagrange equations resulting from the energy density in Eq. (53) with initial conditions

$$q_1(X_1) = \theta(X_1, \theta_0) \cos(\gamma_p) \sin(\gamma_a),$$
$$q_2(X_1) = \theta(X_1, \theta_0) \sin(\gamma_p) \sin(\gamma_a),$$
$$q_3(X_1) = \theta(X_1, \theta_0) \cos(\gamma_a),$$

on $\boldsymbol{q}$ and Eq. (59) on ϕ, for each pair of parameters. Discretizing the parameter space with a grid of 5°, we obtain a polar plot of grain boundary energy shown in Fig. 5b, where a unit vector on the sphere depicts a misorientation axis. Clearly, Fig. 5b shows negligible anisoropy of GB energy with respect to misorientation axis reinforcing the notion of weak-dependence.

In order to demonstrate grain boundary faceting resulting from inclination-dependence due the anisotropic function given in Eq. (64), we consider a 3D simulation of a bicrystal with a spherical grain of radius 30 nm embedded inside a

---

[9] In fact, $\gamma_a = 0$ corresponds to the unit vector along the z-axis irrespective of what γ_p is.

[10] This is analogous to the observation that the KWC energy density with $\epsilon = 0$ is linear in $\nabla\theta$, but the steady state grain boundary energy is concave function (as opposed to a linear function) of the misorientation due to the presence of $g(\phi)$.
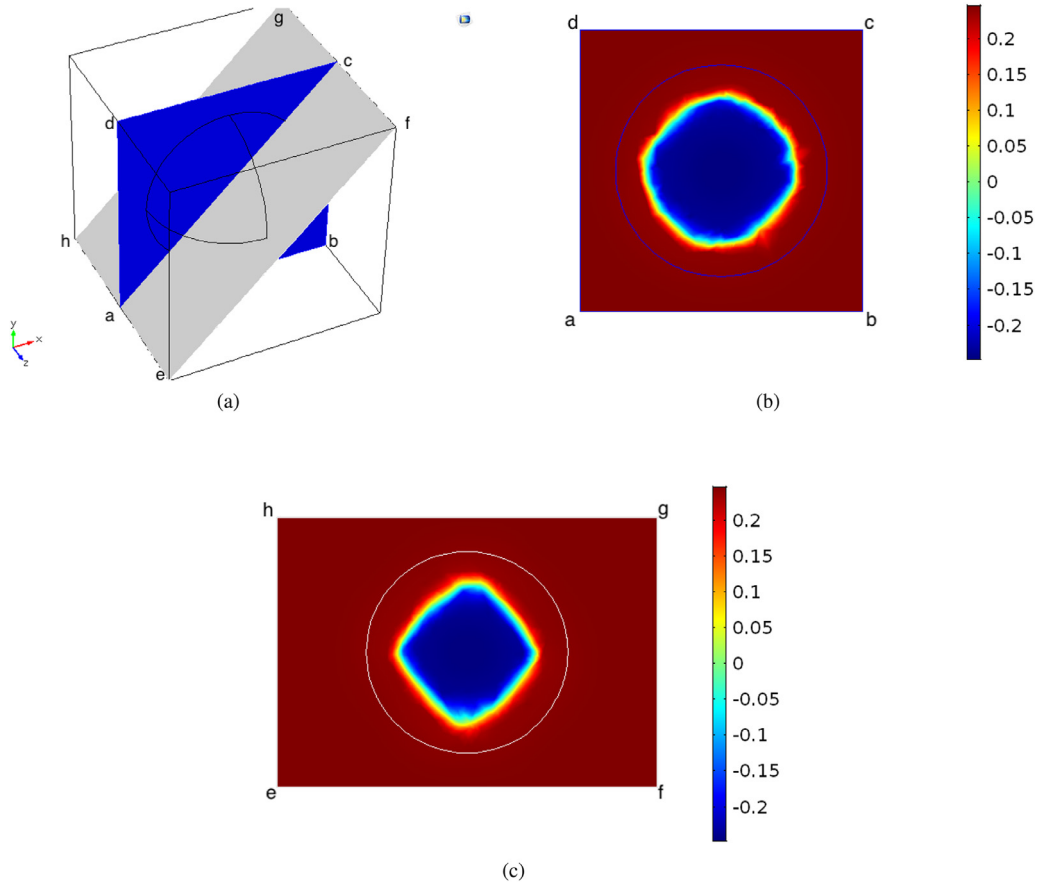
Fig. 6. (a) The *xy* and diagonal planes for which color density plots of q_1 are shown in (b) and (c) respectively. (For interpretation of the references to color in this figure legend, the reader is referred to the web version of this article.)

cubic grain of size 80 nm. The misorientation angle and axis are chosen as 40° and $(1, 1, 0)/\sqrt{2}$ respectively. The domain is decomposed into 31,384 tetrahedral finite elements as shown in Fig. 7a. Fig. 6b and c show a color density plot of q_1 at the $t = 1$s in the *xy* and diagonal planes (as shown in Fig. 6a) respectively. Fig. 6c clearly shows grain boundary faceting while it is not as pronounced in Fig. 6a. This observation is in agreement with the anisotropy of *h*, which exists in the diagonal plane, while it is nonexistent in the *xy* plane. A isosurface plot of the level set $q_1 = 0$ at $t = 1$s in Fig. 7, clearly shows the formation of eight facets. A color density plot of $h(\boldsymbol{R}^{\mathrm{T}}\boldsymbol{n})$, where $\boldsymbol{R}^{\mathrm{T}}\boldsymbol{n}$ is defined in Eq. (52), is also shown on the isosurface. The patterns of maxima and minima in the color plot are consistent with those of the function *h* plotted in Fig. 4. The noise observed in Fig. 6 arises from the coarseness of the mesh, the degree of anisotropy in the energy density, and the parameter ρ that is used to regularize the singular diffusive term in the differential equations associated to the orientation order parameter.

Next, we focus our attention on a comment made at the end of Section 3.5 which says that in a pure twist boundary if the misorientation axis is constant, then the inclination remains constant, while in the presence of a tilt character, the inclination gets diffused. We explore the above-mentioned observation in two simulations of a 2D bicrystal of size 20 nm × 30 nm in the $x − y$ plane with a normal parallel to the *x* axis, and a misorientation angle of 40°. In one case we consider a pure tilt grain boundary with misorientation axis along the *z*-axis, and in the other a pure twist boundary with misorientation axis along the *x*-axis. Since the simulation is in 2D, the energy density in Eq. (53) is expressed in terms of the unknown fields ϕ and θ (as opposed to $\boldsymbol{q}$), while $\boldsymbol{q}$ is expressed in terms of θ as

$$q_1 = q_2 = 0; \quad q_3 = \theta \quad \text{pure tilt}$$
$$q_3 = q_2 = 0; \quad q_1 = \theta \quad \text{pure twist}$$

The initial conditions on ϕ and θ are given by Eq. (59) and Eq. (60) respectively. The isotropic function chosen for this simulation is $h(\boldsymbol{n}) = 1 + 0.5 \sin^2(4\theta)$, where $\sin \theta = n_2$. The domain is decomposed into 4268 triangular finite elements with 168 boundary elements. The system is evolved for 1s until it reaches a steady state. Fig. 8 show level set color density plots of θ at $t = 1$s for a subdomain around the grain boundary, wherein Fig. 8a and b correspond to the pure twist and tilt cases respectively. It is clear from Fig. 8a that the contours of constant θ are along the *y*-axis, which implies the diffused grain
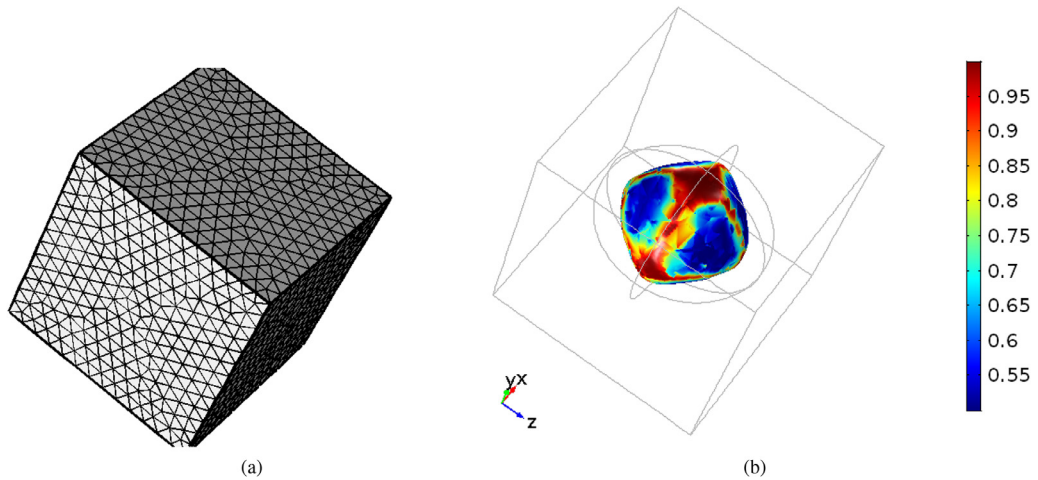
Fig. 7. (a) A 3D mesh of tetrahedral finite elements. (b) An isosurface plot of the level set $q_1 = 0$ at $t = 1$s with color density plot of $h(\boldsymbol{R}^T\boldsymbol{n})$, where $\boldsymbol{R}^T\boldsymbol{n}$ is defined in Eq. (52). (For interpretation of the references to color in this figure legend, the reader is referred to the web version of this article.)
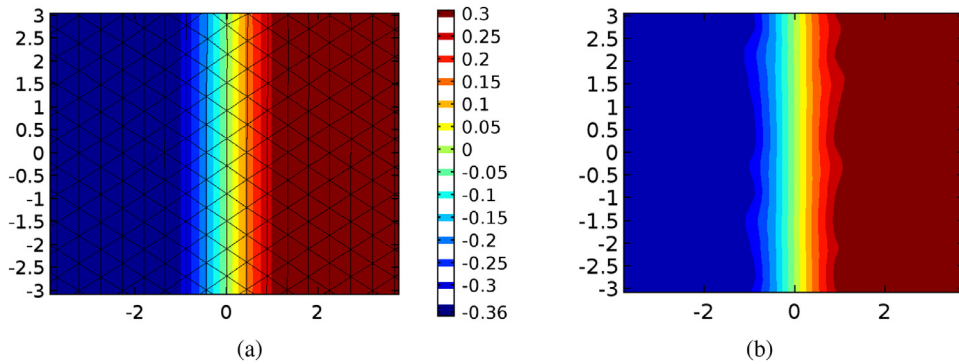

Fig. 8. Color density isosurface plots of θ at steady state resulting from an inclination-dependent model. (a) Corresponds to twist boundary, while (b) corresponds to a tilt boundary demonstrating faceting of the diffused grain boundary away from the origin. Note that the above plot is for a smaller subdomain in the vicinity of the grain boundary. (For interpretation of the references to color in this figure legend, the reader is referred to the web version of this article.)

boundary normal ($:= \nabla\theta/|\nabla\theta|$) is along the x-axis. On the other hand, Fig. 8b shows that the contours of θ are faceted away from the origin, suggesting that the diffused grain boundary normal varies across the grain boundary. In order to identify the reason behind the above-stated difference, we first note that the argument of the function h in the inclination-dependent model is the inclination $\boldsymbol{R}^T\boldsymbol{n}$, and therefore the above-mentioned choice of h attains its minimum when $\boldsymbol{R}^T\boldsymbol{n}$ is parallel to the x axis. In the twist case, since $\boldsymbol{R}^T\boldsymbol{n} = \boldsymbol{n}$, it follows that the diffused grain boundary prefers to remain flat. In the tilt case, if the contours were uniformly parallel to the x-axis, then the inclination varies from $\exp\left(-\frac{\pi}{9}[\boldsymbol{e}^3\times]\right)$ to $\exp\left(\frac{\pi}{9}[\boldsymbol{e}^3\times]\right)$. Therefore, the system adjusts the normals of the contours such that the inclination is as close to $\boldsymbol{e}^1$ as possible, resulting in faceting away from the origin. We note that on an average across the grain boundary, there is no faceting in Fig. 8b. This can also be seen by noting that the mid-plane remains flat. Therefore, the pointwise faceting observed in Fig. 8b is an artifact of the diffuse interface model, and only its average, or the faceting of the mid-plane corresponds to the faceting of a sharp grain boundary. Moreover, Fig. 8b depicts a length scale associated to the facets which should ultimately be related to the length scales in the materials parameters ϵ and α. Further study in this direction is deferred to future work.

Finally, we demonstrate inclination anisotropy under periodic boundary conditions on ϕ and θ in a two-dimensional polycrystal shown in Fig. 9. The orientations of the grains in the polycrystal are in the range $0° - 60°$, and misorientation between grains is at most $15°$.[11] The domain is discretized using 6282 triangular finite elements, with 200 boundary elements. In Fig. 10, we present results of three simulations: (a) full isotropy with $h(\boldsymbol{n}) \equiv 1$, (b) small inclination-anisotropy with $h(\boldsymbol{n}) = 1 - 0.2\sin^2(2\theta)$, and (c) large inclination-anisotropy with $h(\boldsymbol{n}) = 1 - 0.5\sin^2(2\theta)$, where $\sin\theta = n_2$. The effect of increasing the inclination anisotropy is clear from the third column of Fig. 10 which shows grain boundaries with preferential inclination dictated by the anisotropic function. Recall from Section 3.2 the distinction we made between GB inclination and normal. In order to see the distribution of inclination in the polycrystal, we plot in Fig. 11 scaled version of the vector $\boldsymbol{R}^T\boldsymbol{n}$

---

[11] See Admal et al. (2017) for a description of the algorithm used to generate the polycrystal.
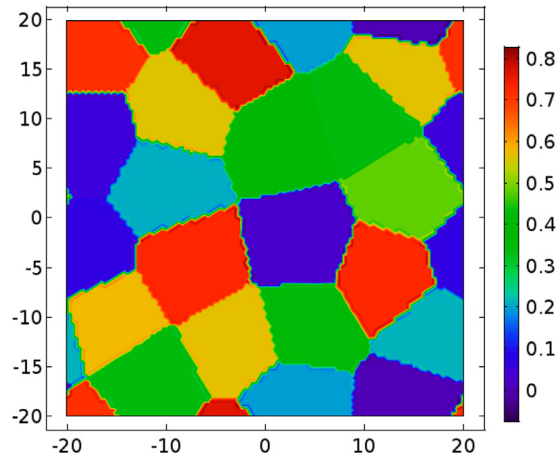
Fig. 9. A color density plot of q_1 for a random polycrystal at $t = 0$. (For interpretation of the references to color in this figure legend, the reader is referred to the web version of this article.)
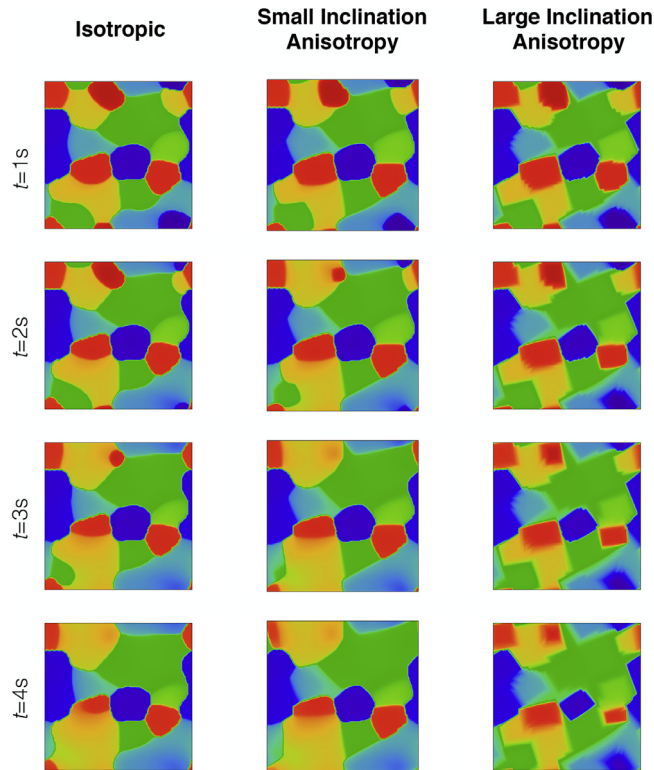

Fig. 10. Color density plots of q_1 corresponding to three simulations: (a) full isotropy with $h(\boldsymbol{n}) \equiv 1$, (b) small inclination-anisotropy with $h(\boldsymbol{n}) = 1 - 0.2 \sin^2(2\theta)$, and (c) large inclination-anisotropy with $h(\boldsymbol{n}) = 1 - 0.5 \sin^2(2\theta)$, where $\sin\theta = n_2$. The legend for the color plots is shown in Fig. 9. (For interpretation of the references to color in this figure legend, the reader is referred to the web version of this article.)

defined in Eq. (52) at $t = 0$ and $t = 3$s. The norm of the plotted vector is chosen to be equal the expression $sg(\phi)h(\boldsymbol{R}^{\mathrm{T}}\boldsymbol{n})|\overline{\boldsymbol{G}}|$ occurring in the energy density. It is clear from Fig. 11a that the initial inclination is quite random. On the other hand, the scaled alignment vector in Fig. 11b is preferentially distributed along the $\pm 45°$ and $\pm 135°$ directions as dictated by the anisotropic function.

4.3. Simulation demonstrating tilt-dependency

In this section, we study the evolution of a tilt-anisotropic grain boundary energy density defined in Section 3.6. Recall that a tilt-anisotropic energy density depends on the misorientation axis and inclination angle only through the tilt angle
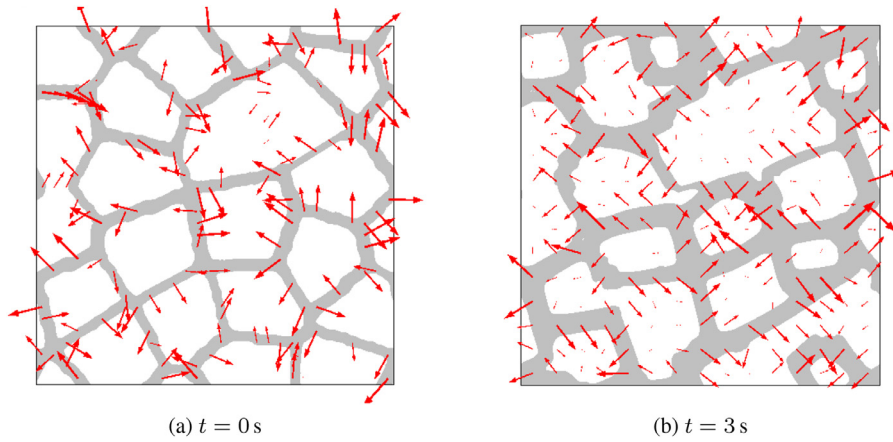
(a) $t = 0\,\mathrm{s}$ (b) $t = 3\,\mathrm{s}$

Fig. 11. A plot of the distribution of a scaled alignment vector field $\boldsymbol{R}^{\mathrm{T}}\boldsymbol{n}$ defined in Eq. (52). The magnitude of the vector field is equal to the term $sg(\phi)h(\boldsymbol{R}^{\mathrm{T}}\boldsymbol{n})|\overline{\boldsymbol{G}}|$ contributing to the energy density. The scaled inclination vector field in (b) clearly demonstrates preferential directions along the $\pm 45°$ and $\pm 135°$ angles as opposed to in (a) where it is randomly distributed.
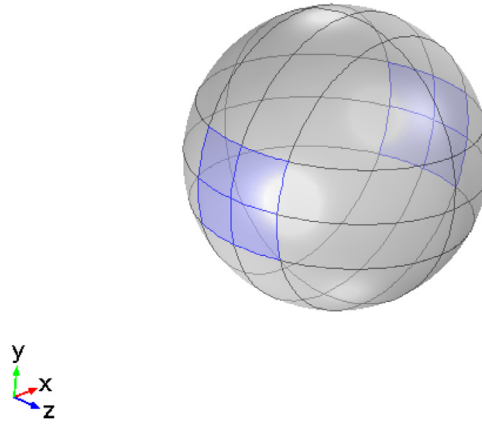
Fig. 12. Simulation of a spherical bicrystal with a tilt-anisotropic grain boundary energy density: Dirichlet boundary conditions, $\boldsymbol{q}(\boldsymbol{X}, t) = (1, 1, 0)\theta(X_1; \theta_0)/\sqrt{2}$ and $\phi(\boldsymbol{X}, t) \equiv 1$ are imposed on parts of the spherical boundary shown in blue.

between them. The tilt-anisotropic function chosen for this study is

$$\bar{h}(\Theta) = (0.5 + 2\cos^2 \Theta(1 - |\cos \Theta|))^2, \tag{67}$$

where the tilt angle Θ is expressed in term of $\overline{\boldsymbol{G}}$ using Eq. (55). $\bar{h}$ attains its minima when the inclination is either 0 or 90°.

In order to explore the anisotropy of $\bar{h}$, we consider a spherical bicrystal of radius 50 nm with a misorientation angle of 40°, misorientation axis along the (1, 1, 0) direction, and grain boundary normal along the x-axis. In other words, we begin with a bicrystal whose tilt angle is equal to 45°. The spherical bicrystal is constructed using the initial conditions

$$q_1(\boldsymbol{X}, 0) = \theta(X_1; \theta_0)/\sqrt{2},$$
$$q_2(\boldsymbol{X}, 0) = \theta(X_1; \theta_0)/\sqrt{2},$$
$$q_3(X_1, 0) = 0.$$

on $\boldsymbol{q}$. The boundary conditions on ϕ and $\boldsymbol{q}$ are of mixed type as depicted in Fig. 12. Fig. 13 shows the color density plots of q_1 at $t = 0$ and 5s. Fig. 13b shows the grain boundary normal rotated counterclockwise by 41° about the z-axis from its original configuration in Fig. 13a. This is close to the expected rotation of 45° as predicted by the anisotropic function given in Eq. (67). In our simulation, we have noted that beyond $t = 5$s, the grain boundary stops rotating and starts slipping away from the equatorial plane. We attribute this to the decrease in the grain boundary area contributing to the energy minimization.[12]

---

[12] Since there is no preferential direction for grain boundary motion away from the equatorial plane, we attribute the observed slipping behavior to symmetry breaking due to the asymmetry in the mesh.
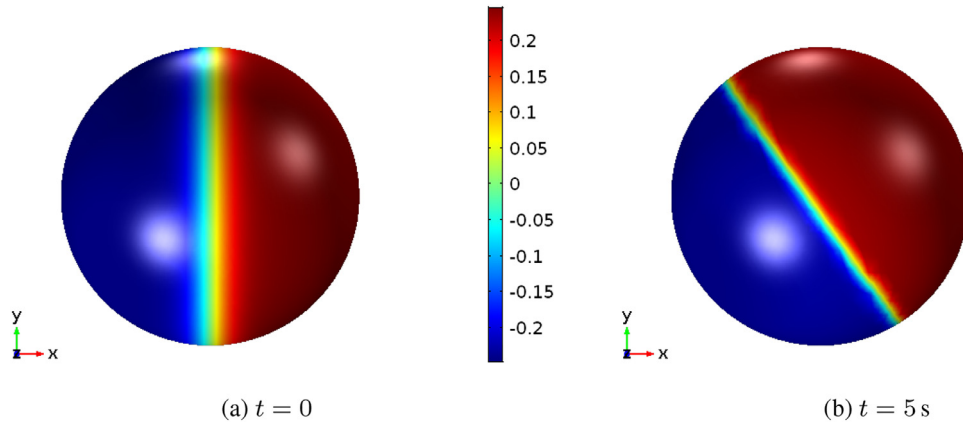
(a) $t = 0$ (b) $t = 5\,\mathrm{s}$

Fig. 13. Color density plot of q_1 in the (a) initial state with grain boundary normal parallel to the x-axis, and (b) at $t = 5$s with normal rotated by $\approx 41°$ about the z-axis. (For interpretation of the references to color in this figure legend, the reader is referred to the web version of this article.)

Before ending this section on numerics, we note that the 3D simulations described here are quite expensive which required us to use a coarse mesh. Although mesh adaptivity may have improved the efficiency, we believe that alternate numerical methods than can handle singular diffusive equations in a more robust manner and take crystal symmetries into account have to be explored. For example, sharp-interface models provide a far more natural framework to describe interfaces. In particular, the works of Gupta and co-workers (Basak and Gupta, 2015a; 2015b; 2016; 2017; Gupta and Steigmann, 2012) (and references therein) serve as an excellent introduction to such models. On the other hand, sharp interface models are traditionally believed to be computationally more demanding. Interestingly, new methods (Esedoglu and Jacobs, 2017; Esedoglu and Otto, 2015; Esedoglu et al., 2017; Ruuth et al., 2001) inspired in image processing are beginning to change this situation.

5. Summary

The KWC model developed by Kobayashi et al. (1998, 2000) is a two-dimensional phase field model used to simulate simultaneous grain boundary motion and grain rotation. Its simplicity in describing grain microstructure using only two phase field variables, ϕ and θ that describe local disorder and grain orientation, respectively, is one of it most salient features compared to well-known multiphase field methods. Existing generalizations of the KWC model are restricted to modeling three-dimensional polycrystals with inclination anisotropy. However, it is known that the GB energy depends not only on the misorientation angle and inclination of the grain boundary but also on the misorientation axis.

In this paper, we have developed a fully-anisotropic three-dimensional KWC model that describes grain boundary energies characterized by misorientation angle, axis and the inclination of the grain boundary. Replacing the order parameter θ that describes orientations in the two-dimensional KWC model with an arbitrary rotation field $\boldsymbol{R}(\boldsymbol{X}) \in SO(3)$, we show using material frame invariance that the KWC energy density should necessarily depend on the tensor $\boldsymbol{G} := \boldsymbol{R}^{\mathrm{T}} \mathrm{Curl}\, \boldsymbol{R}^{\mathrm{T}}$, that encodes misorientation and inclination, and on ϕ. In addition, we have derived frame-invariant non-local definitions of misorientation axis and grain boundary inclination (which is not the same as grain boundary normal) in terms of $\boldsymbol{G}$ which enables us to explore different flavors of anisotropies which include misorientation-axis dependence with inclination-independence and vice versa. In addition, we explore a third kind of anisotropy, referred to as *tilt-anisotropy*, where the grain boundary energy depends only on the misorientation angle and the angle between the misorientation axis and inclination. Using 2D and 3D simulations on bicrystals and polycrystals, we demonstrate all the anisotropies developed in this paper.

Acknowledgements

Appendix A. Interpretation of G from crystal plasticity

The frame-invariant tensor $\boldsymbol{G}$ obtained in Section 3.1 has an interesting interpretation in crystal plasticity. It is in fact the geometrically necessary dislocation (GND) density tensor corresponding to a stress-free polycrystal, which also explains the choice of our notation.
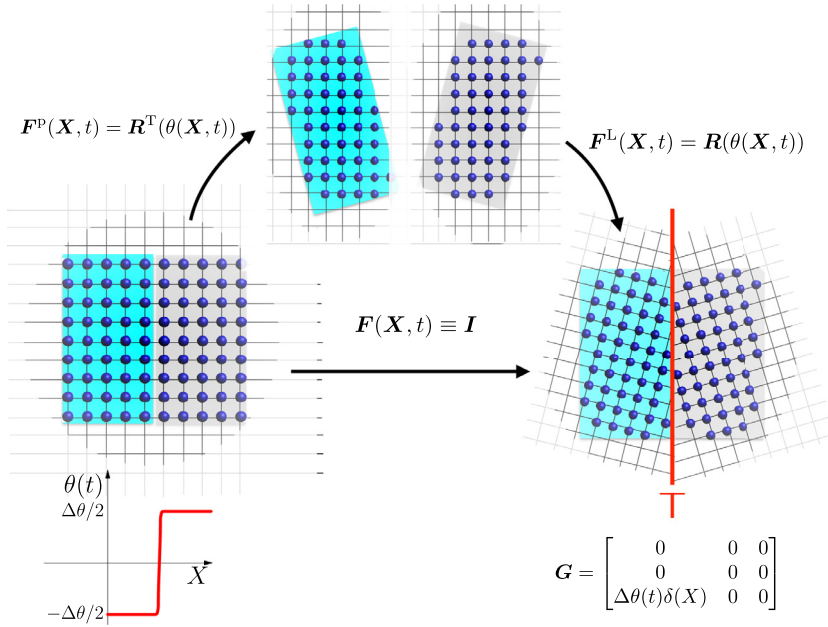
Fig. A.14. An interpretation of $\boldsymbol{G} = \boldsymbol{R}^{\mathrm{T}}\mathrm{Curl}\boldsymbol{R}^{\mathrm{T}}$ from crystal plasticity: $\boldsymbol{G}$ describes the GND density that results in an undeformed stress-free polycrystal at all times due to the special elastic-plastic decomposition $\boldsymbol{F}(\boldsymbol{X},t) = \boldsymbol{F}^{\mathrm{L}}\boldsymbol{F}^{\mathrm{P}}$ with $\boldsymbol{F}^{\mathrm{P}} = \boldsymbol{F}^{\mathrm{LT}}$, and $\boldsymbol{F}^{\mathrm{L}} \in \mathrm{SO}(3)$, a piecewise constant rotation field describing grain orientation, resulting in $\boldsymbol{F}(\boldsymbol{X},t) \equiv \boldsymbol{I}$.

The construction of a stress-free polycrystal is given by Admal et al. (2017, 2018) where a unified framework for polycrystal plasticity with grain boundary evolution is proposed. This construction begins with a multiplicative decomposition of the deformation gradient $\boldsymbol{F} = \boldsymbol{F}^{\mathrm{L}}\boldsymbol{F}^{\mathrm{P}}$, where $\boldsymbol{F}^{\mathrm{L}}$ is the elastic distortion of the lattice, and $\boldsymbol{F}^{\mathrm{P}}$ is the plastic distortion due to crystallographic slip. The construction of the initial stress-free polycrystals is depicted in Fig. A.14, where $\boldsymbol{F}^{\mathrm{L}}(\boldsymbol{X}, 0)$ is taken to be the piecewise constant rotation field describing lattice orientations, while $\boldsymbol{F}^{\mathrm{P}}(\boldsymbol{X}, 0) = \boldsymbol{F}^{\mathrm{LT}}(\boldsymbol{X}, 0)$, resulting in $\boldsymbol{F}(\boldsymbol{X}, 0) = \boldsymbol{I}$ and the initial lattice Lagrangian strain $\boldsymbol{F}^{\mathrm{LT}}\boldsymbol{F}^{\mathrm{L}} - \boldsymbol{I} = \boldsymbol{0}$. Unlike in Admal et al. (2018) where $\boldsymbol{F}$ and $\boldsymbol{F}^{\mathrm{P}}$ are the independent variables, restricting $\boldsymbol{F}^{\mathrm{L}}(\boldsymbol{X}, t)$ to belong to SO(3) and $\boldsymbol{F}^{\mathrm{P}} = \boldsymbol{F}^{\mathrm{LT}}$ for all time, results in the current model describing grain evolution with no deformation. Moreover, from the above interpretation, it is clear that the third-order tensors $\mathcal{G}$ and $\mathcal{B}$ are the torsion and contorsion tensors (see Noll, 1967) respectively.

Appendix B. Choice of $g(\phi)$ in the KWC model

In this section we highlight our reasons for choosing a logarithmic function for $g(\phi)$ as opposed to $g(\phi) = \phi^2$. In Kobayashi and Giga (1999), the authors note that the grain boundary energy as a function of misorientation is of the Read–Shockley type when g is logarithmic, while GB energy is concave for both the choices. In addition, both choices result in a steady state solution for a tricrystal that satisfies the Herring relation, and their sharp interface limits result in motion by curvature.

Despite the above similarities, we now demonstrate using the known analytical *grim-reaper* (Garcke et al., 1999) solution of a tricrystal under periodic boundary condition as shown in Fig. B.15. The KWC parameters used in the simulation are listed in Table B.2. The orientations are chosen such that the horizontal grain boundaries have equal energy densities. Under

Table B.2
KWC parameters used in the model with $g(\phi) = \phi^2$.

	$g(\phi) = \phi^2$
ϵ^2/χ	2.1333×10^{-10} Jm^{-1}
α^2/χ	5.3×10^{-9} Jm^{-1}
s	1.7 Jm^{-2}
$e\chi$	2.1×10^{9} Jm^{-3}
b^ϕ	1×10^{-3} m^3/(Js)
$m^{\boldsymbol{q}}_{\mathrm{max}}$	1×10^{-12} m^3/(Js)
$m^{\boldsymbol{q}}_{\mathrm{min}}$	1×10^{-3} m^3/(Js)
ρ^2	1×10^{13} m^{-2}
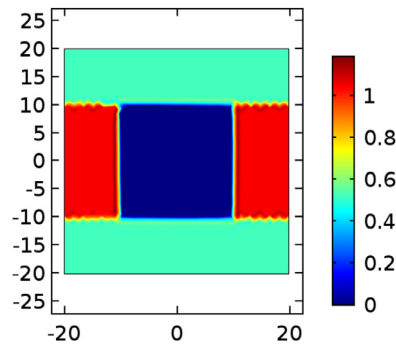
Fig. B.15. A contour plot of the $\theta(\boldsymbol{X}, 0)$ in radians.
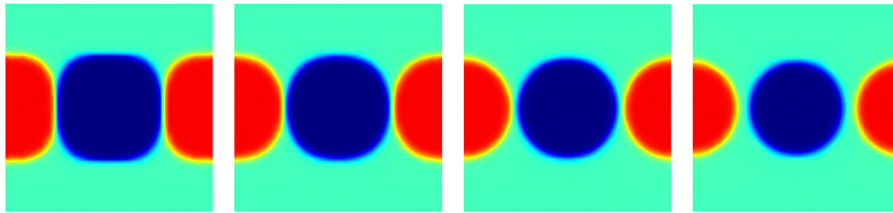

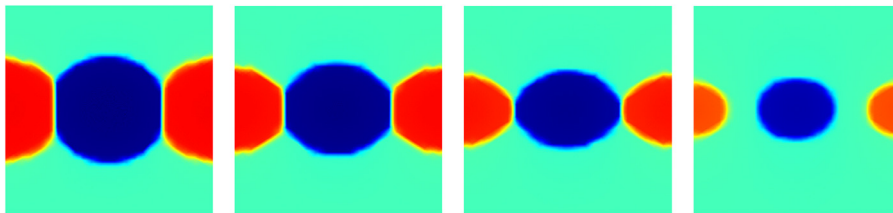**Fig. B.16.** Contour plot of evolution of θ with $g(\phi) = \phi^2$.

Fig. B.17. Contour plot of evolution of θ with $g(\phi) = -2\ln(1 + \epsilon - \phi) + \phi$. In order to avoid the singularity $g(1) = \infty$ when $\epsilon = 0$, we choose $\epsilon = 0.2$.

this constraint, a defining feature of the grim-reaper solution is that the vertical boundaries remain vertical until they shrink to a point, and subsequently the elliptical grains shrink. This feature is demonstrated in Fig. B.17 with a logarithmic g, while a quadratic g shows a completely different evolution as seen in Fig. B.16.

A rigorous study of the above-mentioned differences in grain evolutions is beyond the scope of this paper. Instead, we note form the work of Alicandro et al. (1999) (see Theorem 4.1 in Alicandro et al., 1999) that the KWC functional converges (in the sense of Γ-convergence) to a surface energy function only when $g(1) = \infty$. On the other hand, if $g(1)$ is finite, then the functional converges to a sum of surface and bulk energies. It is remarkable that the above observation is evident only in a Γ-convergence argument as opposed to in the method of matched asymptotics (Lobkovsky and Warren, 2001) to obtain a sharp interface limit.

References

Admal, N.C., Po, G., Marian, J., 2017. Diffuse-interface polycrystal plasticity: expressing grain boundaries as geometrically necessary dislocations. Mater. Theory 1 (1), 6.
Admal, N.C., Po, G., Marian, J., 2018. A unified framework for polycrystal plasticity with grain boundary evolution. Int. J. Plast. 106, 1–30.
Alicandro, R., Braides, A., Shah, J., 1999. Free-discontinuity problems via functionals involving the L^1-norm of the gradient and their approximations. Interfaces Free Bound. 1 (1), 17–37. doi:10.4171/IFB/2.
Anderson, M., Srolovitz, D., Grest, G., Sahni, P., 1984. Computer simulation of grain growth-I. Kinetics. Acta Metall. 32 (5), 783–791.
Arnold, V.I., 1966. Sur la géométrie différentielle des groupes de lie de dimension infinie et ses applicationsa lhydrodynamique des fluides parfaits. Ann. Inst. Fourier 16 (1), 319–361.
Ask, A., Forest, S., Appolaire, B., Ammar, K., 2018a. A cosserat–phase-field theory of crystal plasticity and grain boundary migration at finite deformation. Continuum Mech. Thermodyn. doi:10.1007/s00161-018-0727-6.
Ask, A., Forest, S., Appolaire, B., Ammar, K., Salman, O.U., 2018b. A cosserat crystal plasticity and phase field theory for grain boundary migration. J. Mech. Phys. Solids 115, 167–194.
Basak, A., Gupta, A., 2015a. Simultaneous grain boundary motion, grain rotation, and sliding in a tricrystal. Mech. Mater. 90, 229–242.
Basak, A., Gupta, A., 2015b. A three-dimensional study of coupled grain boundary motion with junctions. In: Proceedings of the Royal Society of London A: Mathematical, Physical and Engineering Sciences, vol. 471. The Royal Society, p. 20150127.
Basak, A., Gupta, A., 2016. Plasticity in multi-phase solids with incoherent interfaces and junctions. Continuum Mech. Thermodyn. 28 (1–2), 423.
Basak, A., Gupta, A., 2017. Influence of a mobile incoherent interface on the strain-gradient plasticity of a thin slab. Int. J. Solids Struct. 108, 126–138.

Belytschko, T., Gracie, R., Ventura, G., 2009. A review of extended/generalized finite element methods for material modeling. Modell. Simul. Mater. Sci. Eng. 17 (4), 043001.

Bulatov, V. V., Reed, B. W., Kumar, M., 2013. Anisotropy of interfacial energy in five dimensions. arXiv:1305.1282

Chen, L.-Q., 2002a. Phase-field models for microstructure evolution. Annu. Rev. Mater. Res. 32 (1), 113–140.

Chen, L.-Q., 2002b. Phase-field models for microstructure evolution. Annu. Rev. Mater. Res. 32 (1), 113–140.

Chen, L.-Q., Yang, W., 1994. Computer simulation of the domain dynamics of a quenched system with a large number of nonconserved order parameters: the grain-growth kinetics. Phys. Rev. B 50 (21), 15752.

De Giorgi, E., Ambrosio, L., 1988. Un nuovo tipo di funzionale del calcolo delle variazioni. Atti della Accademia Nazionale dei Lincei. Classe di Scienze Fisiche, Matematiche e Naturali. Rendiconti Lincei. Matematica e Applicazioni 82 (2), 199–210.

Dorr, M., Fattebert, J.-L., Wickett, M., Belak, J., Turchi, P., 2010. A numerical algorithm for the solution of a phase-field model of polycrystalline materials. J. Comput. Phys. 229 (3), 626–641. doi:10.1016/j.jcp.2009.09.041.

Esedoglu, S., Jacobs, M., 2017. Convolution kernels and stability of threshold dynamics methods. SIAM J. Numer. Anal. 55 (5), 2123–2150.

Esedoglu, S., Otto, F., 2015. Threshold dynamics for networks with arbitrary surface tensions. Commun. Pure Appl. Math. 68 (5), 808–864.

Esedoglu, S., Jacobs, M., Zhang, P., 2017. Kernels with prescribed surface tension & mobility for threshold dynamics schemes. J. Comput. Phys. 337, 62–83.

Frolov, T., Setyawan, W., Kurtz, R.J., Marian, J., Oganov, A.R., Rudd, R.E., Zhu, Q., 2018a. Grain boundary phases in BCC metals. Nanoscale 10 (17), 8253–8268.

Frolov, T., Zhu, Q., Oppelstrup, T., Marian, J., Rudd, R.E., 2018b. Structures and transitions in BCC tungsten grain boundaries and their role in the absorption of point defects. Acta Mater. 159, 123–134. doi:10.1016/j.actamat.2018.07.051.

Garcke, H., Nestler, B., Stoth, B., 1999. A multiphase field concept: numerical simulations of moving phase boundaries and multiple junctions. SIAM J. Appl. Math. 60 (1), 295–315.

Gránásy, L., Pusztai, T., Warren, J.A., 2004. Modelling polycrystalline solidification using phase field theory. J. Phys. 16 (41), R1205.

Gupta, A., Steigmann, D.J., 2012. Plastic flow in solids with interfaces. Math. Methods Appl Sci. 35 (15), 1799–1824.

Han, J., Thomas, S.L., Srolovitz, D.J., 2018. Grain-boundary kinetics: a unified approach. Prog. Mater. Sci. 98, 386–476.

Henry, H., Mellenthin, J., Plapp, M., 2012. Orientation-field model for polycrystalline solidification with a singular coupling between order and orientation. Phys. Rev. B 86, 054117. doi:10.1103/PhysRevB.86.054117.

Hirouchi, T., Tsuru, T., Shibutani, Y., 2012. Grain growth prediction with inclination dependence of ⟨110⟩ tilt grain boundary using multi-phase-field model with penalty for multiple junctions. Comput. Mater. Sci 53 (1), 474–482. doi:10.1016/j.commatsci.2011.08.030.

Holm, E.A., Glazier, J.A., Srolovitz, D.J., Grest, G.S., 1991. Effects of lattice anisotropy and temperature on domain growth in the two-dimensional potts model. Phys. Rev. A 43 (6), 2662.

Horita, Z., Smith, D.J., Nemoto, M., Valiev, R.Z., Langdon, T.G., 1998. Observations of grain boundary structure in submicrometer-grained Cu and Ni using high-resolution electron microscopy. J. Mater. Res. 13 (2), 446–450.

Inkson, B., Mulvihill, M., Möbus, G., 2001. 3D determination of grain shape in a FeAl-based nanocomposite by 3D FIB tomography. Scr. Mater. 45 (7), 753–758.

Janssens, K.G., Olmsted, D., Holm, E.A., Foiles, S.M., Plimpton, S.J., Derlet, P.M., 2006. Computing the mobility of grain boundaries. Nat. Mater. 5 (2), 124.

Kacher, J., Robertson, I., Nowell, M., Knapp, J., Hattar, K., 2011. Study of rapid grain boundary migration in a nanocrystalline Ni thin film. Mater. Sci. Eng. 528 (3), 1628–1635.

Karma, A., Rappel, W.-J., 1996. Phase-field method for computationally efficient modeling of solidification with arbitrary interface kinetics. Phys. Rev. E 53 (4), R3017.

Khater, H., Serra, A., Pond, R., Hirth, J., 2012. The disconnection mechanism of coupled migration and shear at grain boundaries. Acta Mater. 60 (5), 2007–2020.

Kim, H.-K., Kim, S.G., Dong, W., Steinbach, I., Lee, B.-J., 2014. Phase-field modeling for 3D grain growth based on a grain boundary energy database. Modell. Simul. Mater. Sci. Eng. 22 (3), 034004.

Kobayashi, R., Giga, Y., 1999. Equations with singular diffusivity. J. Stat. Phys. 95 (5), 1187–1220. doi:10.1023/A:1004570921372.

Kobayashi, R., Warren, J.A., 2005. Extending phase field models of grain boundaries to three dimensions cond-mat/0502398. Available from http://cds.cern.ch/record/823487.

Kobayashi, R., Warren, J.A., 2005b. Modeling the formation and dynamics of polycrystals in 3d. Physica A 356 (1), 127–132.

Kobayashi, R., Warren, J.A., Carter, W.C., 1998. Vector-valued phase field model for crystallization and grain boundary formation. Physica D 119 (3–4), 415–423.

Kobayashi, R., Warren, J.A., Craig Carter, W., 2000. A continuum model of grain boundaries. Physica D 140 (1–2), 141–150. doi:10.1016/S0167-2789(00)00023-3.

Krill Iii, C., Chen, L.-Q., 2002. Computer simulation of 3-D grain growth using a phase-field model. Acta Mater. 50 (12), 3059–3075.

Lobkovsky, A., Warren, J., 2001. Sharp interface limit of a phase-field model of crystal grains. Phys. Rev. E 63 (5), 051605.

Ma, A., Roters, F., Raabe, D., 2006. On the consideration of interactions between dislocations and grain boundaries in crystal plasticity finite element modeling–theory, experiments, and simulations. Acta Mater. 54 (8), 2181–2194.

Mecozzi, M., Eiken, J., Santofimia, M., Sietsma, J., 2016. Phase field modelling of microstructural evolution during the quenching and partitioning treatment in low-alloy steels. Comput. Mater. Sci 112, 245–256. doi:10.1016/j.commatsci.2015.10.048.

Miyoshi, E., Takaki, T., 2016. Extended higher-order multi-phase-field model for three-dimensional anisotropic-grain-growth simulations. Comput. Mater. Sci 120, 77–83. doi:10.1016/j.commatsci.2016.04.014.

Moelans, N., Blanpain, B., Wollants, P., 2008a. Quantitative phase-field approach for simulating grain growth in anisotropic systems with arbitrary inclination and misorientation dependence. Phys. Rev. Lett. 101 (2), 025502.

Moelans, N., Blanpain, B., Wollants, P., 2008b. Quantitative phase-field approach for simulating grain growth in anisotropic systems with arbitrary inclination and misorientation dependence. Phys. Rev. Lett. 101, 025502. doi:10.1103/PhysRevLett.101.025502.

Molodov, D., Shvindlerman, L., Gottstein, G., 2003. Impact of grain boundary character on grain boundary kinetics. Zeitschrift für Metallkunde 94 (10), 1117–1126.

Molodov, K.D., Molodov, D.A., 2018. Grain boundary mediated plasticity: on the evaluation of grain boundary migration - shear coupling. Acta Mater. 153, 336–353. doi:10.1016/j.actamat.2018.04.057.

Noll, W., 1967. Materially uniform simple bodies with inhomogeneities. Arch. Ration. Mech. Anal. 27 (1), 1–32. doi:10.1007/BF00276433.

Olmsted, D.L., Buta, D., Adland, A., Foiles, S.M., Asta, M., Karma, A., 2011. Dislocation-pairing transitions in hot grain boundaries. Phys. Rev. Lett. 106 (4), 046101.

Olmsted, D.L., Foiles, S.M., Holm, E.A., 2009. Survey of computed grain boundary properties in face-centered cubic metals: I. grain boundary energy. Acta Mater. 57 (13), 3694–3703.

Pusztai, T., Bortel, G., Gránásy, L., 2005. Phase field theory of polycrystalline solidification in three dimensions. EPL 71 (1), 131.

Reina, C., Sandoval, L., Marian, J., 2014. Mesoscale computational study of the nanocrystallization of amorphous Ge via a self-consistent atomistic phase-field model. Acta Mater. 77, 335–351.

Runnels, B., Beyerlein, I.J., Conti, S., Ortiz, M., 2016. An analytical model of interfacial energy based on a lattice-matching interatomic energy. J. Mech. Phys. Solids 89, 174–193.

Runnels, B.S., 2016. A Model for Energy and Morphology of Crystalline Grain Boundaries with Arbitrary Geometric Character. California Institute of Technology Ph.D. thesis..

Ruuth, S.J., Merriman, B., Xin, J., Osher, S., 2001. Diffusion-generated motion by mean curvature for filaments. J. Nonlinear Sci. 11 (6), 473–493. doi:10.1007/s00332-001-0404-x.

Simone, A., Duarte, C., Van der Giessen, E., 2006. A generalized finite element method for polycrystals with discontinuous grain boundaries. Int. J. Numer. Methods Eng. 67 (8), 1122–1145.

Steinbach, I., 2009. Phase-field models in materials science. Modell. Simul. Mater. Sci. Eng. 17 (7), 073001.

Steinbach, I., Pezzolla, F., 1999. A generalized field method for multiphase transformations using interface fields. Physica D 134 (4), 385–393.

Steinbach, I., Pezzolla, F., Nestler, B., Seeßelberg, M., Prieler, R., Schmitz, G.J., Rezende, J.L., 1996. A phase field concept for multiphase systems. Physica D 94 (3), 135–147.

Sursaeva, V., Straumal, B., 2005. Influence of grain boundary inclination on the grain boundary and triple junction motion in Zn. Materialwissenschaft und Werkstofftechnik 36 (10), 528–532.

Suwa, Y., Saito, Y., 2005. Phase field simulation of the effect of anisotropy in grain boundary energy on growth kinetics and morphology of grain structure. Mater. Trans. 46 (6), 1208–1213.

Taheri, M.L., Rollett, A.D., Weiland, H., 2004. In-situ quantification of solute effects on grain boundary mobility and character in aluminum alloys during recrystallization. In: Materials Science Forum, vol. 467. Trans Tech Publ, pp. 997–1002.

Taheri, M.L., Sebastian, J.T., Reed, B.W., Seidman, D.N., Rollett, A.D., 2010. Site-specific atomic scale analysis of solute segregation to a coincidence site lattice grain boundary. Ultramicroscopy 110 (4), 278–284.

Thomas, S.L., Chen, K., Han, J., Purohit, P.K., Srolovitz, D.J., 2017. Reconciling grain growth and shear-coupled grain boundary migration. Nat. Commun. 8 (1), 1764.

Upmanyu, M., Srolovitz, D.J., Lobkovsky, A., Warren, J.A., Carter, W., 2006. Simultaneous grain boundary migration and grain rotation. Acta Mater. 54 (7), 1707–1719.

Wei, Y., Anand, L., 2004. Grain-boundary sliding and separation in polycrystalline metals: application to nanocrystalline fcc metals. J. Mech. Phys. Solids 52 (11), 2587–2616.

Wolf, U., Ernst, F., Muschik, T., Finnis, M.W., Fischmeister, H.F., 1992. The influence of grain boundary inclination on the structure and energy of Σ3 grain boundaries in copper. Philos. Mag. A 66 (6), 991–1016. doi:10.1080/01418619208248003.

Zefran, M., Kumar, V., Croke, C., 1996. Choice of Riemannian metrics for rigid body kinematics. In: ASME 24th Biennial Mechanisms Conference, vol. 2.